

Immunological and cardio-vascular pathologies associated with SARS-CoV-2 infection in golden syrian hamster

Zaigham Abbas Rizvi¹, Rajdeep Dalal^{1#}, Srikant Sadhu^{1#}, Yashwant Kumar³, Tripti Srivastava², Sonu Kumar Gupta³, Suruchi Agarwal³, Manas Ranjan Tripathy¹, Amit Kumar Yadav³, Guruprasad R. Medigeshi², Amit Kumar Pandey², Sweety Samal², Shailendra Asthana², Amit Awasthi^{1*}

¹Immuno-biology Lab, Infection and Immunology centre, Translational Health Science and Technology Institute, NCR-Biotech Science Cluster, 3rd Milestone, Faridabad-Gurgaon Expressway, Faridabad-121001, Haryana, India

²Infection and Immunology centre, Translational Health Science and Technology Institute, NCR-Biotech Science Cluster, 3rd Milestone, Faridabad-Gurgaon Expressway, Faridabad-121001, Haryana, India

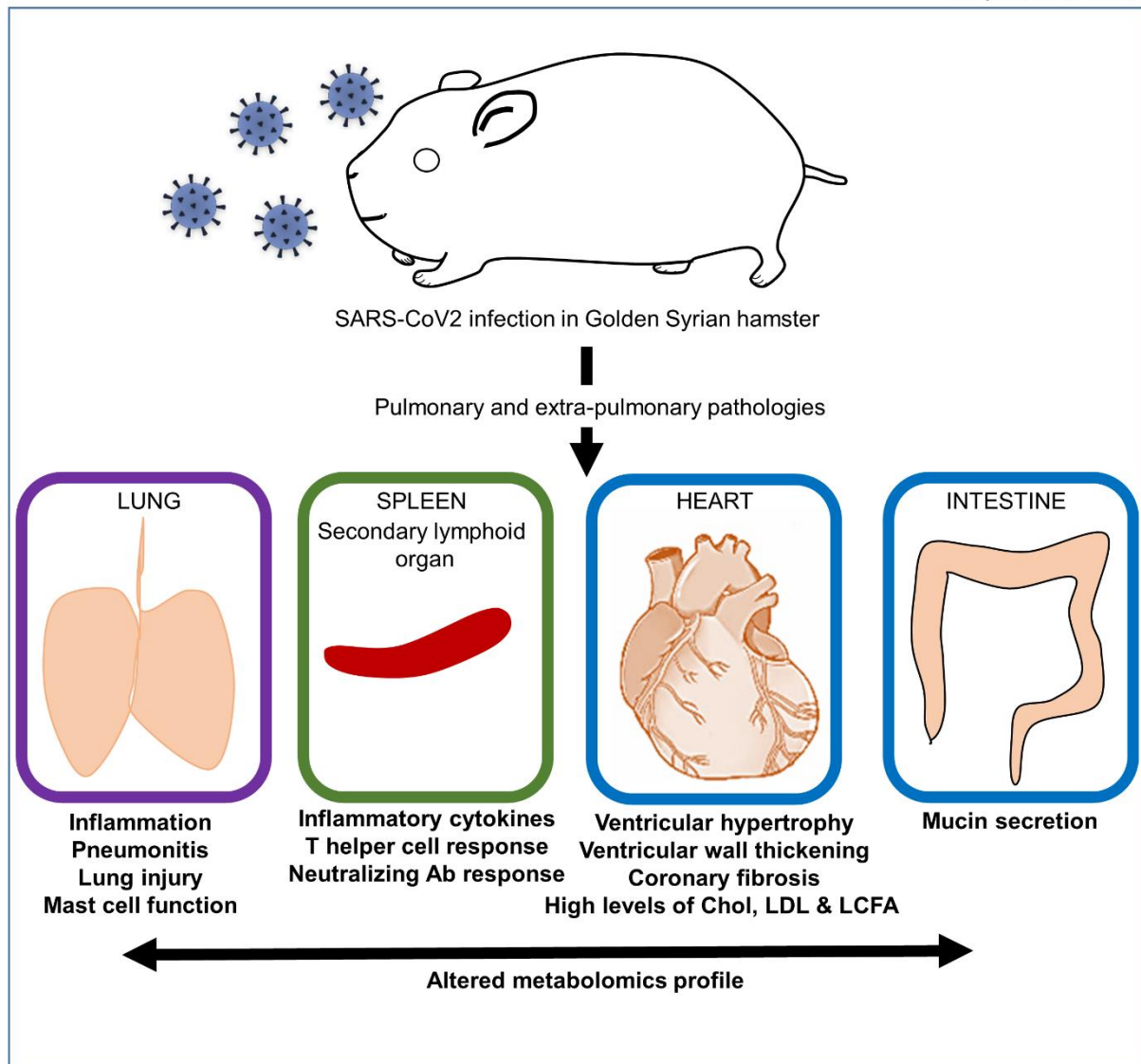
²Non-communicable disease centre, Translational Health Science and Technology Institute, NCR-Biotech Science Cluster, 3rd Milestone, Faridabad-Gurgaon Expressway, Faridabad-121001, Haryana, India

Equal contribution

***Corresponding author:**

Amit Awasthi, PhD
Immuno-biology Laboratory,
Translational Health Science & Technology Institute (THSTI)
3rd Milestone, Faridabad-Gurgaon Expressway, Faridabad, Haryana, India 121001
Email: aawasthi@thsti.res.in
Phone: +91-129-287-6482, fax: +91-129-287-6500

Graphical Abstract



Summary

Severe acute respiratory syndrome coronavirus (SARS-CoV)-2 infection in golden Syrian hamster (GSH) causes lungs pathology and resembles to human corona virus disease (Covid-19). Extra-pulmonary pathologies and immunological parameters of SARS-CoV-2 infection remained undefined in GSH. Using *in silico* modelling, we identified the similarities between human and hamster angiotensin-converting enzyme-2 (ACE-2), neuropilin-1 (NRP-1) that bind to receptor-binding domain (RBD) and S1 fragment of spike protein of SARS-CoV-2. SARS-CoV-2 infection led to lung pathologies, and cardiovascular complications (CVC) marked by interstitial coronary fibrosis and acute inflammatory response. Serum lipidomic and

metabolomic profile of SARS-CoV-2-infected GSH revealed changes in serum triglycerides (TG) and low-density lipoprotein (LDL), and alterations in metabolites that correlated with Covid19. Together, we propose GSH as an animal model to study SARS-CoV-2 infection and its therapy associated with pulmonary and extra-pulmonary pathologies.

Keywords: SARS-CoV2, Covid-19, hamster, cardio-vascular, immunology, lipidomics, metabolomics, lung pathology.

Introduction

First reported in Wuhan, China in December 2019, SARS-CoV-2 has infected nearly 0.9 % of the total world population with around 2.17 % mortality rate as of January 2021 (<https://covid19.who.int/>). Symptomatic COVID-19 is typically characterized by symptoms ranging from mild to acute respiratory distress which is associated with cytokine storm (Chen and Li, 2020; Verity et al., 2020). Other extra-pulmonary symptoms ranging from CVC, inflammation, coagulopathies, multiple organ damage and neurological disorders have been described in patients with mild to severe covid-19 infection (Chen and Li, 2020; Lamers et al., 2020; Mao et al., 2020; Nishiga et al., 2020; Wu et al., 2020; Xiao et al., 2020; Xydakis et al., 2020). The severity of covid-19 is governed by several host-virus factors such as dose of virus, route of viral entry, gender, age and comorbidity (Chen and Li, 2020; Sungnak et al., 2020; Wang et al., 2020). The RBD of spike (S) glycoprotein of SARS-CoV2 engages with angiotensin-converting enzyme 2 (ACE2), a cellular receptor expressed on host cells, which facilitates the viral entry into the host cell. Upon the engagement of ACE2 with SARS-CoV2, cellular transmembrane protease ‘serine 2’ (TMPRSS2) mediates the priming of viral S protein by cleaving at S1/S2 site induces the fusion of viral and host cellular membranes, thus facilitating viral entry into the cells (Hoffmann et al., 2020). Lower levels of surface expression of ACE2 in respiratory and olfactory epithelial cells, however indicates a possibility of

involvement of other co-receptors, which may be crucial for the infectivity of SARS-CoV2. Neuropilin-1 (NRP-1), which is abundantly expressed on the surface of endothelial and epithelial cells and binds to furin cleaved substrates, has been shown to facilitate SARS-CoV2 infectivity (Cantuti-Castelvetri et al., 2020; Daly et al., 2020). S1 fragment of the spike protein cleaved by furin has been shown to directly bind to NRP1 expressed on the cell surface, and thus promote the viral interaction with ACE2 (Cantuti-Castelvetri et al., 2020; Daly et al., 2020).

Various non-human primates and small animal models have been described to study the pathogenesis and transmission of SARS-CoV2 infection. SARS-CoV2 is inefficient in infecting mice due to structural differences in mouse ACE2 as compared to human ACE2, thus wild type mice are not the natural host to study SARS-CoV2 induced pathologies (Chan et al., 2020). On the other hand, Syrian hamster, which was previously described as a model for SARS-CoV infection, has recently gained much attention as a suitable model for studying SARS-CoV2 infection (Chan et al., 2020; Sia et al., 2020). Remarkably, hamsters have been shown to be infected through intranasal, oral and ophthalmic routes by SARS-CoV2 with respectively descending lung viral load and pathologies (Imai et al., 2020). Moreover, airborne transmission of SARS-CoV2 infection to uninfected animals and its reduction by the use of surgical mask barrier between the cages corroborates with the clinical cases of SARS-CoV2 making Syrian hamster as a standard model for pre-clinical screening of effective therapeutics and vaccine candidates. Despite several reports on hamsters describing the SARS-CoV2 pathology in the lung and pre-clinical evaluation of therapeutics against it, no study has focused on cardiovascular complications associated with lipidomics and metabolomics changes and related immunopathologies in SARS-CoV2 infected hamsters.

In the current study, we demonstrate using *in-silico* modelling, that host-virus interaction has a striking similarity between humans and hamsters that involves TMPRSS2-mediated priming

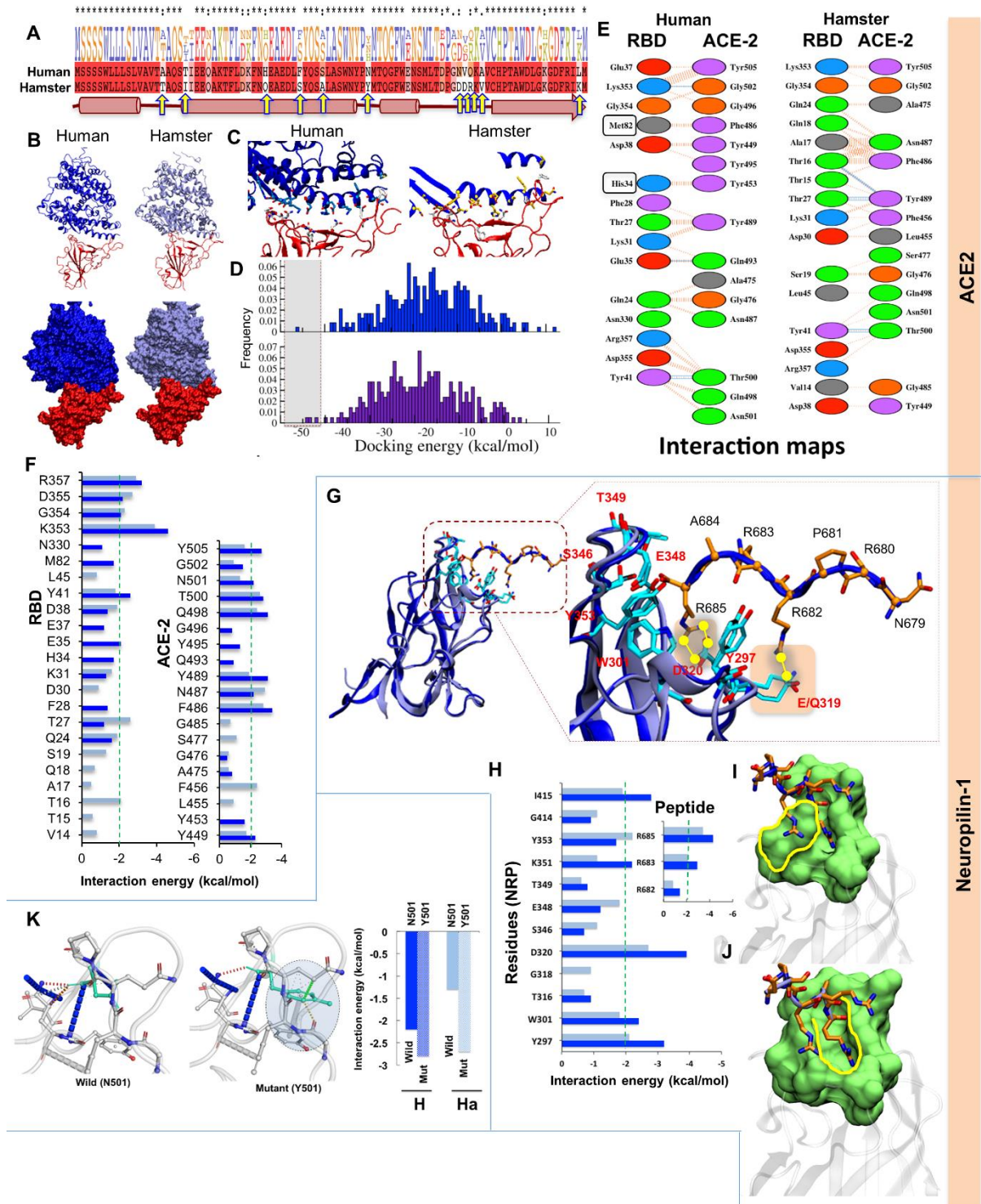
of S protein, binding of S1 peptide with NRP-1 and subsequent binding of RBD to ACE2. Intranasal infection of SARS-CoV2 in hamster resulted in high lung viral load with significantly elevated lung injury on 2 and 4 dpi. Furthermore, our data shows aggressive immune activation characterized by heightened expression of inflammatory cytokines on 2 and 4dpi. Strikingly, SARS-CoV2 infection in the hamster leads to significant interstitial coronary fibrosis on day 7 and 14 dpi characterized by thickening of ventricular walls and interventricular septum. These cardiovascular changes were associated with increased serum triglycerides, low-density lipoprotein (LDL), cholesterol, high-density lipoprotein (HDL) on 4 dpi, and a marked increase in long chain fatty acids (LCFAs) on 7dpi. Finally, we found marked changes in the metabolomics profile characterized by elevated N-acetylneuraminate and allantoin which corroborated with the covid19 severe patients metabolomic profile. Taken together, here we describe hamster as an excellent model to study cardiovascular complications resulting from SARS-CoV2 infection and the underlying changes in lipidomics and metabolomics serum profile which may serve as a suitable pre-clinical model to study not only pulmonary damages associated with SARS-CoV2 infection but also extra-pulmonary pathologies.

Results

In silico interaction predicts similarities in the host-virus interaction between hamster and human

Interaction of SARS-CoV-2 RBD with host ACE2 receptor, TMPRSS protease and NRP-1 is critical for virus entry into epithelial cells. However, the similarities of these interactions between human (hu) and GSH (ha) remained unexplored. To compare residues of hu and ha ACE2 that interact with RBD of SARS-CoV2, structure-guided sequence alignment was performed with their respective sequences (**Figures S1A and 1A**). The overlay of crystal of

Figure 1



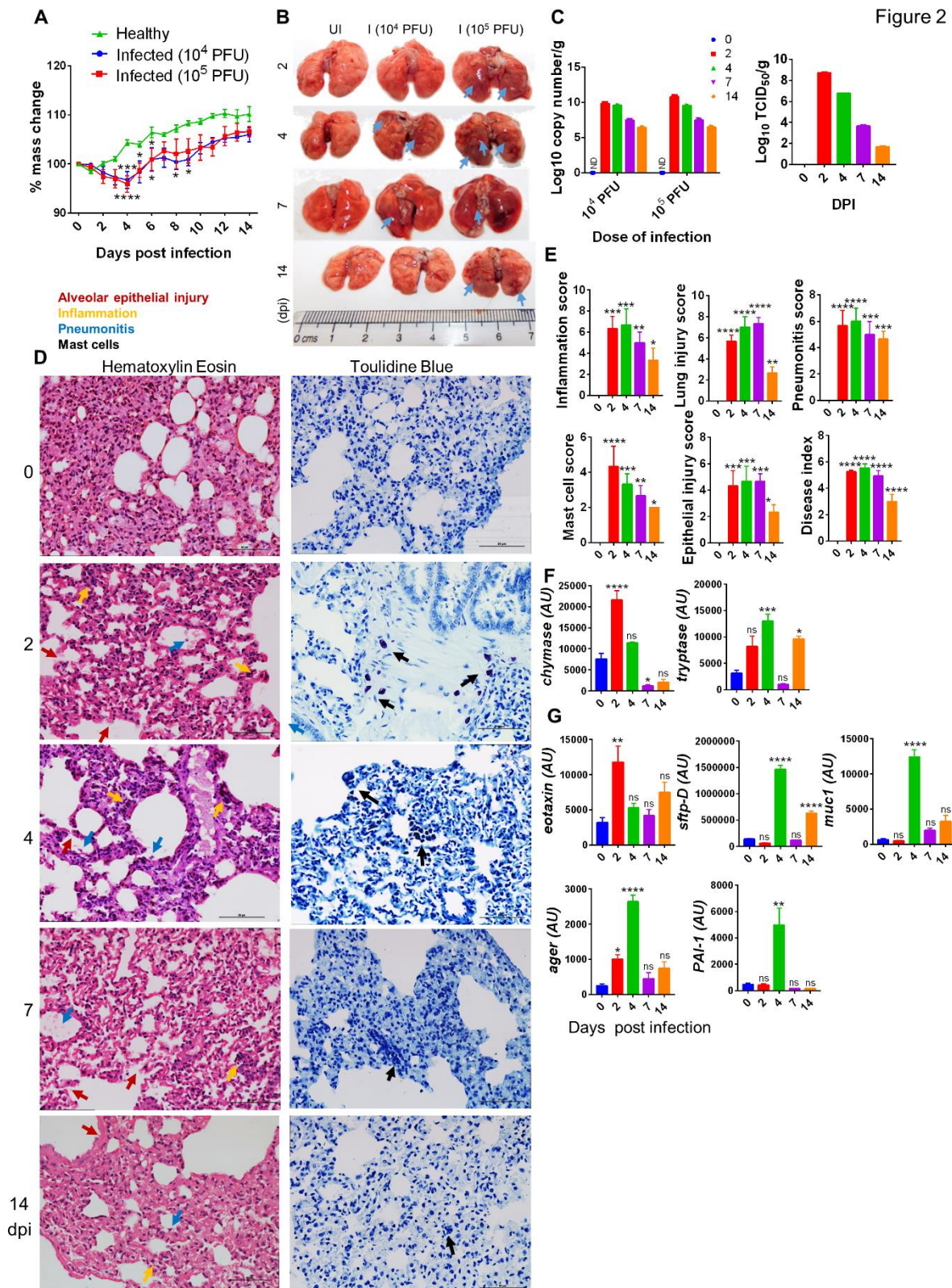
108

109 huACE2 with modelled haACE2 was 1.2 Å, indicating the high structural resemblance. At

110 interface a total of 17 and 16 residues of the RBD are in contact with 20 residues of hu and ha

ACE2, respectively (**Figures 1B-1E**). The notable features that was common for both hu/ha ACE2 interfaces with RBD was the networks of hydrophilic interactions like hydrogen bonds (H-bonds) and salt bridges between Lys31 and Lys353 of ACE2 with Glu35 and Asp38 of RBD (**Figures 1E and 1F**). Aromatic residues of RBD, Tyr449, Tyr453, Phe456, Phe486, Tyr489, Tyr495 and Tyr505, contributing to binding affinity remained common for both hu/ha ACE2 (**Figure 1F**). Together, SARS-CoV2 RBD with hu/ha ACE2 interfaces shared a substantial similarities in the buried surface area, the number of interacting residues and hydrophilic interaction. hu/ha TMPRSS2 structurally looks very similar (**Figure S1B**). NRP-1, which bind to S1 fragment of spike protein, facilitates SARS-CoV2 entry within the cells (Cantuti-Castelvetri et al., 2020; Daly et al., 2020). Hu and ha NRP-1, the C-terminal R685 of the CendR peptide, interacts identically with S1 fragment of spike protein residues, Y297, W301, T316, D320, S346, T349 and Y353 (**Figures 1G, 1H and 1I**). The R682 and R685 sidechains S1 fragment of spike protein engages with NRP-1 sidechains of Y297 and Y353 via stacked cation- π interactions (**Fig. 1I and J**). In huNRP-1, the residues interacting from C-endR are R685 making H-bonds with residues Asp320, Ile415, Tyr353, Thr349 and Ser346 of S1 fragment while in haNRP-1, the R685 remains stable but with less number of H-bonds with residues Trp297, Gly318, Asp320, Tyr353 and Thr349. The other common interactions in terms of hydrophobic contacts are with residues Thr316, Gly414, and Trp301. Glu348 and Lys351 contributed only in huNRP-1 while Ser346 in haNRP-1. Among mutations at RBD, the cause of stable Y501 over N501 was also compared in hu/ha, as Y501 gain additional bonding with tyrosine residues (41@ACE2, 355@RBD) and H-bond with Arg353 (**Figure 1K**).

SARS-CoV2 infection results in pulmonary pathologies characterized by inflammation and lung injury



135

136 These *in silico* data provides a comparative molecular insight of SARS-CoV2 interaction and

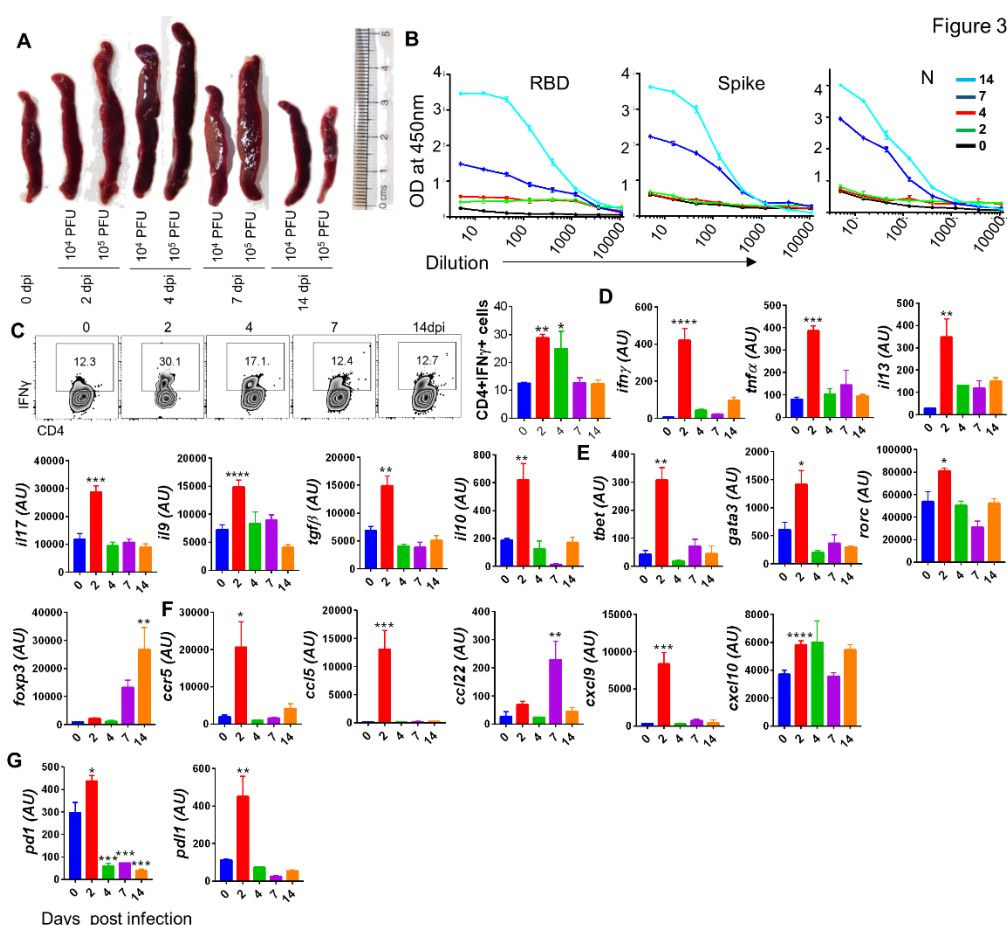
137 entry in GSH showing similarities with human infection. Further, a decrease in body mass had

been reported in the initial phase of SARS-CoV2 infection. In line, intranasal SARS-CoV2 infection in GSH showed a gradual body mass loss peaking (~10% as compared to uninfected) at 4 days post infection (dpi) with 10^4 and 10^5 plaque forming unit (PFU), in line with earlier reports (**Figure 2A**) (Chan et al., 2020; Sia et al., 2020). This was accompanied by gross lungs morphological changes characterized by pneumonitis regions with high viral load ($\sim 10.5 \log_{10}$ copy number/g (lung mass) and TCID₅₀ at 2 dpi that gradually decreased at later time points marking the recovery of the animals (**Figures 2B and 2C**). Covid-19 is marked by severity of pneumonia, lung injury and influx of activated immune cells (Afrin et al., 2020; Chen and Li, 2020; Moore and June, 2020). In line with this, histological analysis revealed elevated disease index score characterized by scores of inflammation, epithelial injury, lung injury and pneumonitis with elevated infiltration of granulocytes and mast cells on 2, 4 and 7 dpi (**Figures 2D and 2E**). Consistently, mRNA expression of mast cells signature enzymes, chymase and tryptase, was increased on 2 and 4 dpi corroborating mast cell enrichment (**Figure 2F**). Furthermore, the expression of eotaxin, a CC chemokine and a potent chemoattractant for airway eosinophils and mast cells that is particularly elevated in asthma and allergy conditions, was upregulated at 2 dpi (**Figure 2G**). The expression of other lung injury markers like mucin (muc-1: marker of respiratory infections), surfactant protein-D (sftp-D: acute lung injury marker), advanced glycation end product (AGER: pro-inflammatory pattern recognition receptor) and plasminogen activator inhibitor-I (PAI-1: a key factor for lung fibrosis) was upregulated at 4 dpi (**Figure 2G**). Collectively, these data indicated elevated lung pathologies characterized by the upregulation of lung injury markers in SARS-CoV2 infection.

SARS-CoV2 infection in hamster results in aggressive immune activation

Most SARS-CoV2 infection studies in hamster have focused on pathological changes and viral load in different organs. Moreover, Covid19 patients have shown an aggressive immune

activation leading to cytokine storm (Mathew et al., 2020; Moore and June, 2020; Verity et al.,

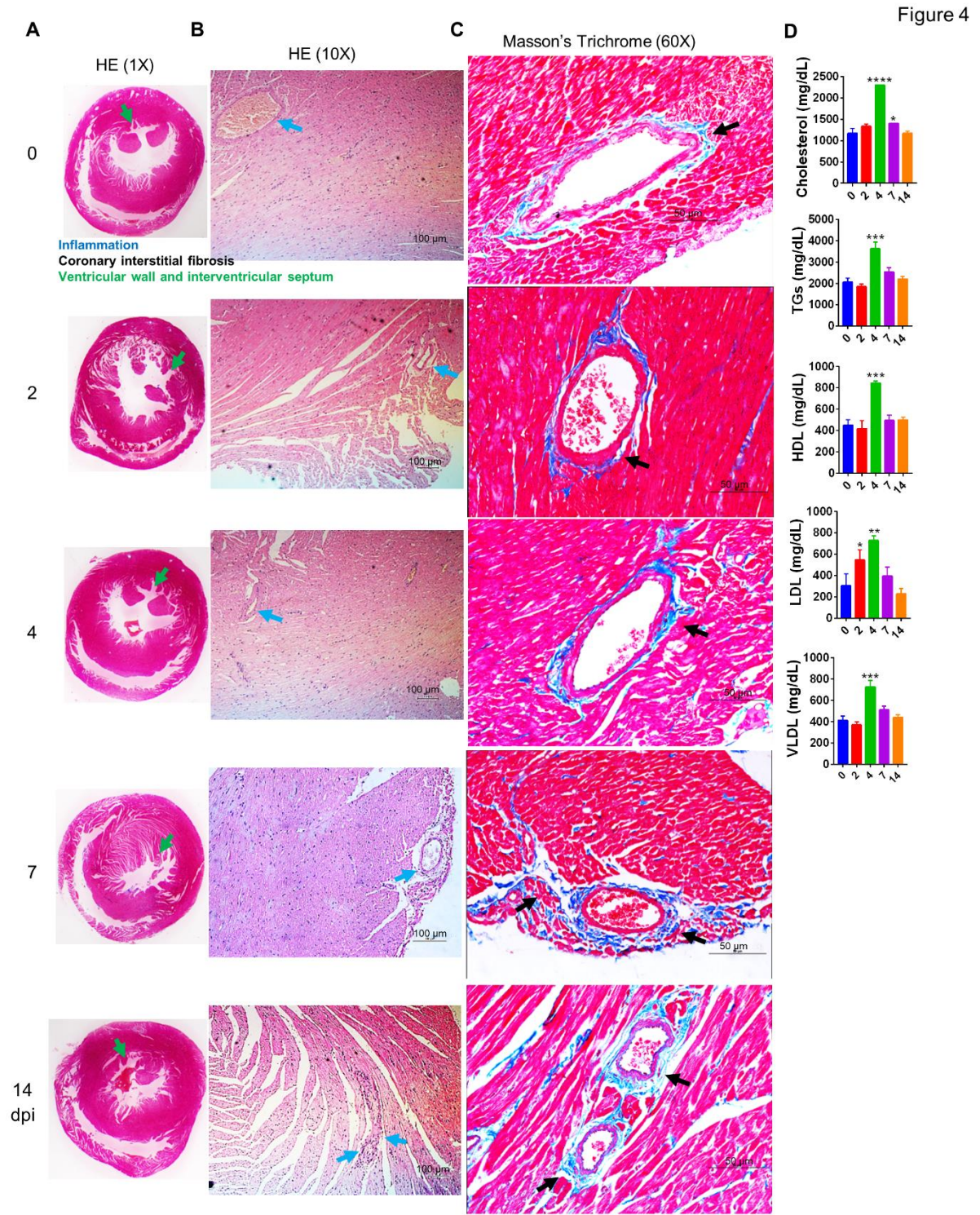


2020). Further, pathological changes of the lung and other organs have been attributed to the acute inflammatory response caused by SARS-CoV2 infection. Consistently, profound splenomegaly was observed in infected animals with ~60% increase in spleen size on 4 dpi for 10⁵ PFU SARS-CoV2 infected hamsters as compared to the healthy control (**Figure 3A**), indicating that splenomegaly could be an indicator of disease severity to define the efficacy of therapeutics against SARS-CoV2 infection in GSH. To corroborate with the recovery response, serum IgG titre for viral proteins, RBD, Spike and N protein was determined. As compared to low dose, high dose of infection generate higher IgG titre against RBD (**Figure S2A**). The RBD, Spike (prefusion S2P), and N protein ELISA detected the corresponding antibodies in challenged animals as early as 7 dpi. The serum endpoint antibody titres against RBD, spike and N protein were detected as early as 7 dpi with the titre 1:3610, 1:405 and 1:330

respectively, the titre of these antibodies was further enhanced to 1:8900, 1:550 and 1:660 at 14 dpi (**Figure 3B**), indicating for a steady recovery of infection. In addition, antigen-specific frequency of CD4⁺IFN γ ⁺ cells was elevated (~2.5 fold) without affecting the frequency of CD4⁺T cells at 2 dpi as compared to uninfected GSH (**Figures 3C and S2B**). To define cellular response particularly T helper (Th) cell response against SARS-CoV2 infection in GSH, we performed mRNA expression of crucial cytokines, chemokines, transcription factors and checkpoint inhibitors, and found an increased expression of Th1, Th2, Th9 and Th17 cells signature cytokines at the peak of infection (i.e. 2 dpi) viz IFN γ , tumor necrosis factor (TNF)- α ; interleukin (IL)-13; IL-9, IL-17A along with their respective transcription factors, T-bet, GATA3, RAR-related orphan receptor (ROR)-c (Grifoni et al., 2020; Mathew et al., 2020). However, transcription factor forkhead box protein (Foxp)-3 was found to be elevated at 14 dpi suggesting activation of regulatory T (Tregs) cells at the senescence of infection. Interestingly, Tregs cytokines IL-10 and transforming growth factor (TGF)- β sets in much early at 2 dpi which maybe to counterbalance aggressive inflammatory reaction (**Figures 3D and 3E**). We also found boosted expression of IL-6 and inducible nitric oxide synthase (inos) at 2 dpi, indicative of cytokine storm and oxidative environment (**Figure S2C**). Further, we found elevated expression of C-C chemokine receptor (CCR5) and C-C motif chemokine ligand (CCL)-5, at 2 dpi, which regulates T cell function and chemotaxis. CCL-22, which is essential for Treg-DCs cross talk, was elevated at 7 dpi. The expression of CXCL9 and CXCL-10, which are crucial for effector T cell trafficking and activation, and have been described as a biomarker for CVC, was upregulated at 2 dpi (**Figure 3F**). PD-1 and its ligand, PDL-1, were also found to be upregulated at the onset of infection, suggesting induction of checkpoints to suppress aggressive immune activation (**Figure 3G**). These data suggests that SARS-CoV2 infection in GSH induces an acute immune activation, chemotaxis and expansion of immune

cell population at the peak that resembles to a pattern of cytokine storm reported in Covid19 (Afrin et al., 2020; Moore and June, 2020).

Defining cardiovascular pathologies in SARS-CoV2 infected hamsters



Myocardial injury occurs in around 25% of hospitalized covid-19 patients that includes

thromboembolic diseases and cases of arrhythmia (Giustino et al., 2020). Interplay between host-virus interaction through ACE2-RBD and its impact on renin-angiotensin system (RAS) and host immunological response are in central to the development of CVC (Giustino et al., 2020). However, lack of suitable SARS-CoV2 animal model has been a limitation for studying cardiovascular related complications arising. Acute inflammatory response, CXCL9/10 upregulation and oxidative environment made us rationale that SARS-CoV2 infection in GSH may lead to CVC. Indeed, 7 dpi heart showed marked ventricular hypertrophy (**Figure S3A**) associated with reduced ventricular space characterized by thickening of ventricular walls and interventricular septum at 7 and 14 dpi (**Figure 4A**). The increased ventricular walls thickening at 7 and 14 dpi was marked by increased inflammation surrounding the coronary artery and elevated interstitial coronary fibrosis (**Figure 4B and 4C**). Interestingly, increased fibrosis is an established pathophysiological stage in majority of CVC (Kong et al., 2014; Travers et al., 2016). Further, since CVC are often linked with perturbed serum lipid profile, we reasoned that cardio-vascular pathologies of SARS-CoV2 in hamsters maybe related to changes in circulating lipid molecules. Indeed, serum lipid profile showed elevated cholesterol, TGs, HDL, LDL and VLDL levels at 4 dpi (**Figure 4D**). Together, our results provide evidence for CVC arising due to SARS-CoV2 infection in hamsters.

Long chain fatty acid accumulation in SARS-CoV2 infection hamsters maybe responsible for CVC

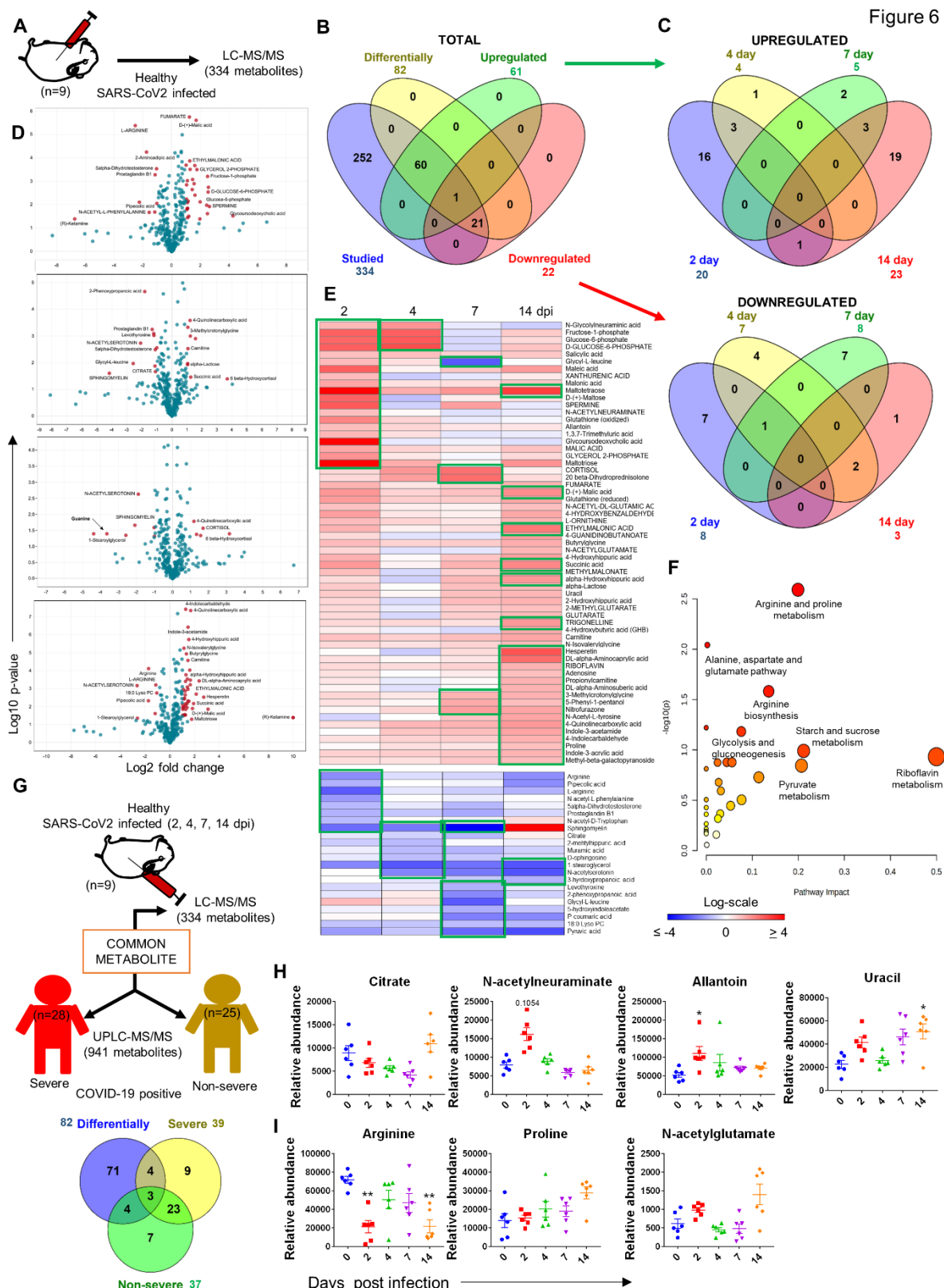
Since our preliminary data revealed perturbations in lipid profile of SARS-CoV2 infected hamster, we set out to do a detailed characterization of modulation in the abundance of lipid moieties at different time points of infection through ultra-performance liquid chromatography-tandem mass spectrometry (UPLC-MS/MS) to identify the potential lipid biomarkers associated with cardio-vascular pathologies. Our LC-MS/MS data identified 831 lipid molecules from the hamster serum samples (**Figure 5A**). These 831 lipid molecules were 11

hexocylceramide (Hex-Cer), 31 lysophosphatidylcholine (LPC), 19
 lysophosphatidylethanolamine (LPE), 7 lysophosphatidylinositol (LPI), 105 oxidized (Ox),
 107 phosphatidylcholine (PC), 41 phosphatidylethanolamine (PE), 7 phosphatidylglycerol
 (PG), 38 phosphatidylinositol (PI), 141 ether bond containing lipid (Plasmenyl), 4
 phosphatidylserine (PS), 56 sphingomyelin (SM), 5 saturated lipids (SO), 135 triglycerides
 (TG) (**Figure 5B**). Interestingly, 7 dpi showed the most distinct PCA distribution plot that
 corroborated well with the severe 7 dpi cardio-vascular pathology of SARS-CoV2 infected
 hamsters (unpublished data). Next in order to identify the uniquely perturbed lipid molecules
 on 2, 4, 7 and 14 dpi hamster serum samples, we carried out t-test analysis compared to
 uninfected (0 dpi) control. Resulting volcano plots for 2, 4, 7 and 14 dpi (top to bottom)
 indicates log2 fold change of lipid molecules which were differentially regulated as compared
 to the uninfected control (**Figure 5C**). Importantly, 275 lipids were differentially regulated as
 identified by *t*-test analysis (described in methods section) of which 65 lipids molecules were
 up-regulated while 208 were downregulated as identified by log2 fold change by volcano plots
 (**Figure 5D and Table S1**). Further, heatmap for log2 fold change values for differentially
 regulated lipids and for normalized relative abundance showed distinct clusters of lipids at
 different time points (**Figures 5E and S3B**). Our lipidomics data show that unsaturated TGs
 (4-11 double bonds (db)), plasmanly-PE (1-6 db) and plasmanyl-TGs (1-3 db) were uniquely
 upregulated during infection while saturated TGs (1-3 db), DGs, oxidized lipids, PC, PE and
 PI were down regulated. However, both saturated TGs and oxidized lipids, implicated in CVC,
 were downregulated upon infection. Interestingly, upregulated TGs were mainly long chain
 fatty acid (LCFAs) TGs while majority of downregulated TGs were medium chain fatty acid
 (MCFAs) TGs that we reasoned as mediators of CVC in hamsters as increased LCFAs and
 decreased MCFAs are associated with increased risks of heart diseases (Labarthe et al., 2008).
 In addition to CVC, SARS-CoV2 can infect human gastro-intestinal tract cells expressing

ACE2 and cause associated pathologies (15). Moreover, severe SARS-CoV2 infection is also known to cause multiple organ failure affecting kidney, liver, brain (16). To evaluate extra-pulmonary pathophysiological of infected GSH, we carried out detailed histological analysis of these major organs. Results show a significantly increase in mucin expression at 2, 4 and 7 dpi hamsters indicative of onset of inflammation and gastro-intestinal injury (**Figure S4A**). However, there were no gross changes observed in brain, liver and kidney of infected as compared to uninfected hamsters at 2 dpi (**Figure S4B**).

Metabolomics changes in SARS-CoV2 infection in hamsters and identification of potential metabolic biomarkers for disease pathophysiology

Emerging literature has suggested that the metabolomic changes are associated with Covid-19 patients (Shen et al., 2020). Attempts were made to identify signature metabolite that could help in predicting the disease severity and progression. In order, to find a clinical correlation of metabolomics signatures associated with SARS-CoV2 infection in hamster, we carried out detailed metabolomics analysis for 2, 4, 7 and 14 dpi infected serum samples and compared it with uninfected (0 dpi) control. A schematic flow for the metabolomics study is shown in (**Figure 6A**). Corroborating with highest viral load and immune response, 2 dpi showed distinct PCA distribution (**Figure S5A**). *t-test* analysis identified 82 differentially regulated metabolites out of 334, of which 61 metabolites were upregulated and 22 were downregulated (described in method section) (**Figures 6B and 6C**). The volcano plots indicating log2 fold change in metabolites abundance vs uninfected control was exploited to plot heatmap showing unique clusters (**Figures 6D, 6E and Table S2**). The relative abundance of individual serum samples have been depicted as heatmap (**Figure S5B**). Collectively riboflavin pathway, arginine and proline metabolism were significantly impacted by these differentially regulated metabolites (**Figure 6F**). Next, correlation analysis with *Bo Shen et al 2020* metabolomics profile of severe and non-severe covid19 patients depicted as (**Figure 6G**) (Shen et al., 2020) revealed an



282

283 overlap of 21 metabolites with non-covid 19 metabolites, 37 with non-severe, 37 with severe

284 and 5 with severe vs non-severe metabolites shown as a Venn diagram (Figures S5C and

S5D). Importantly, 4 metabolites were common between severe covid19 patients and our differentially regulated metabolites viz Citrate, N-acetylneuraminate, allantoin and uracil, while 3 metabolites, Arginine, proline and N-acetylglutamate, were common between severe, non-severe and our differentially regulated metabolites (**Figures 6G, 6H and 6I**). Remarkably, N-acetylneuraminate and Allantoin were highly upregulated at 2 dpi in our study and corroborated well with severe disease profile in covid19 patients (**Figure 6H**). Moreover, both N-acetylneuraminate and allantoin have been previously described as CVD biomarkers (Zhang Lei et al., 2018). Together, based on the previously published study we identify and propose biomarkers for disease severity in hamsters and also identify mediators for extra-pulmonary manifestations.

Discussion

Pulmonary as well as extra-pulmonary clinical and histopathological changes associated with SARS-CoV2 infection in human had been described by several groups (Moore and June, 2020; Nishiga et al., 2020; Wang et al., 2020). Golden Syrian hamster as a pre-clinical SARS-CoV2 infection model was recently shown to mimic viral entry and replication naturally similar to human and therefore is often favoured over transgenic mouse model (Chan et al., 2020; Imai et al., 2020; Lee et al., 2020; Sia et al., 2020). The infection in hamster causes lung pathologies which resembles that of the human lung marked by pneumonitis, inflammation and alveolar epithelial injury (Chan et al., 2020; Lee et al., 2020; Sia et al., 2020). This is not a surprising observation as hACE2 and haACE2 receptors had previously been shown to share major sequence homology. Such similarities between hACE2 and haACE2 strongly point to interaction with SARS-CoV2 receptor binding domain (RBD) structures with a similar trend of binding affinity. Our *in silico* data on haACE2 extends the previous knowledge providing greater insight into the interaction established between haACE2 and RBD protein. Moreover, the interacting residues and changes in interaction energy is strikingly similar between hamster

and human and as a result the furin cleaved S subunit could enter the interacting groove of haNRP-1 and prime it for the interaction with ACE2 in a manner similar to human. Importantly, the host-virus interaction of SARS-CoV2 infection in hamster was found to be similar to human infection for the recently reported SARS-CoV2 mutant. Since, *in silico* data was suggestive of similarity in SARS-CoV2 interaction in hamsters and humans, which corroborates well with intranasal infection and subsequent lung viral load in hamsters as reported by previous studies. Since, increased viral load in the lungs is reflective of lung pathologies and have been shown to induce inflammation and injuries in the clinical cohorts, we reasoned that consistent pathophysiological changes maybe occurring in the hamsters as well. In line, we observed profound pneumonitis, inflammation and alveolar epithelial injury upon histological assessments of the lung. Our data show that lung pathologies long persists after the virus clearance from the lung since we observed high pathological score on 7 dpi. This corroborates with the clinical cases in which it has been observed that lung pathophysiology is perturbed long after the recovery of infected individuals. We also found significant upregulation of the expression of lung injury markers on 2 or 4 dpi corroborating the lung pathologies.

Viremia is an important pathological characteristic of SARS-CoV2 infection in humans, further SARS-CoV2 is known to shed viral proteins which could be circulating in the serum long after the virus is cleared off. The host responds to these pathogenic factors by producing IgG antibodies for its effective neutralization. Therefore, we also evaluated the antibody titre for viral proteins viz RBD, Spike and N protein in the sera of the infected hamsters. We found that IgG response to SARS-CoV2 was most profound on 7 and 14 dpi which corroborates well with the notion of antibody priming and expansion. An important arm of the host response against SARS-CoV2 depends on immune recognition of the invading pathogen and its activation. Interestingly, we also observed profound splenomegaly in infected animals on 2 and 4 dpi pointing at an active and immune cells stimulation and proliferation. Further, numerous clinical

studies have shown that SARS-CoV2 infection is characterized by cytokine storm which is responsible for lung pathologies and respiratory distress in severe cases. Important mediators of inflammatory response such as IFN γ , IL6, IL17A, etc have been shown to be produced in robust amount and drive the escalated immune regulation. Our data show dramatic increase in Th1 cell response mediated by IFN γ for *in vitro* stimulated 2 dpi splenocytes. qPCR studies revealed a similar activation pattern for several inflammatory cytokines and chemokines along with immuno-regulatory transcription factors indicating that the immune activation sets in quite early during infection and maybe playing a role in pathological damages associated with lung and other organs during infection.

SARS-CoV2 can affect cardiovascular system which results in inflammation, endothelial activation and microvascular thrombosis. The cardiovascular complications have particular been reported in co-morbidity patients and may lead to life threatening condition. Since, there is a lack of knowledge about the cardio-vascular complication arising from SARS-CoV2 infection in hamster we carried out a detailed histological analysis to monitor the changes occurring in and around cardiomyocytes of the heart muscle. Interestingly, we found profound thickening of the ventricular and interventricular septum with marked depression in ventricular space capacity on 7 and 14 dpi heart samples. These changes were accompanied by deposition of fibrous mass around coronary artery and inflammation which is believed to be one of the major causes of cardio-vascular complication and arrhythmia. Observation of cardio-vascular complication on 7 and 14 dpi was a remarkable finding which hinted strongly at extra-pulmonary damages caused by SARS-CoV2. It also pointed at soluble mediators of host or the pathogen which could lead to cardio-vascular complication long after the virus is cleared off from the lungs. One such important mediators of cardio-vascular diseases are serum lipid molecules. This prompted us to carry out lipidomics profiling of the serum of the infected and uninfected hamster samples. We found global changes in the lipid profile associated with

infection but quite remarkably 7 and 14 dpi samples produced the largest clusters of altered lipid molecules which was in perfect agreement with out heart histology data. Interestingly, SARS-CoV2 infected hamster serum samples showed an increase in LCFAs accumulation as compared to MCFAs which have been described as biomarkers of CVC and heart failure.

In addition to lack of data on the extra-pulmonary changes associated with SARS-CoV2 infection in hamster, no studies have been done to evaluate the metabolomics changes occurring in the hamster infected with SARS-CoV2 infection. Therefore we carried out both reverse phase and HILIC phase LC-MS/MS analysis for metabolomics changes in infected hamsters. Moreover, we also observed striking similarities between the metabolomics profile of hamsters compared with the clinical database. When compared to the metabolomic profile of severe and non severe Covid19 patients, 7 metabolites were found to be common in hamsters. These metabolites were citrate, N-acetylneuraminate, allantoin, uracil. Proline, arginine and N-acetylglumate out of which N-acetylneuraminate and allantoin showed positive correlation with severe covid19 metabolomic profile with sharp peak in abundance at 2dpi. Both allantoin and N-acetylneuraminate increased abundance have been shown to be biomarkers for increased heart risk. Together, our data provides first insight into the key metabolites which could be used as the biomarkers for the efficient and rapid evaluation of SARS-CoV2 disease severity.

As of now hamster model for SARS-CoV2 has been described as a suitable model to study lung pathologies and clinical parameter such as body wight changes. However, a robust hamster animal model which mimics the histopathological changes in extra pulmonary regions upon SARS-CoV2 infection has not been evaluated. Therefore, in the current study we provide a detailed insight into the cardio-vascular and immunopathological changes associated with SARS-CoV2 describing the lipidomic and metabolomics changes in the infected hamsters and

provide the first proof-of-concept (PoC) study for a robust pre-clinical model for pulmonary and extra-pulmonary pathologies associated with SARS-CoV2 infection.

Acknowledgments

Financial support to AA laboratory from THSTI core and Translational Research Program (TRP) and Department of Biotechnology (DBT) and DST-SERB. We acknowledge IDRF (THSTI) for the support at ABSL3 facility. Luvas (University of Hisar) and CDRI for providing the hamster for the study. Small animal facility and Immunology Core for providing support in experimentation. ILBS for support in histological analysis and assessment. RCB microscopy facility for microscopic examination of histology slide. We thank Dr. Gagandeep Kang, CMC Vellore for providing the support for this project. The following reagent was deposited by the Centers for Disease Control and Prevention and obtained through BEI Resources, NIAID, NIH: SARS Related Coronavirus 2, Isolate USA-WA1/2020, NR-52281. AKY is supported by DBT-Big Data Initiative grant (BT/PR16456/BID/7/624/2016) and the Translational Research Program (TRP) at THSTI funded by DBT.

Author Contributions

Conceived, designed and supervised the study: AA; Designed and performed the experiments: AA, ZAR, RD, SS; ABSL3 procedures: ZAR, RD, SS, AKP; *in silico* study: SA; qPCR primer designing and analysis: ZAR; FACS: ZAR; Histology and analysis: ZAR, MRT; Metabolomics: YK, ZAR, SKG; Lipidomics: YK, ZAR, SKG; ELISA: TS; Viral load: GPM; Virus stock and TCID50: SSamal; Omics analysis: AKY, SAgarwal, ZAR, RD, SS; Contributed reagents/materials/analysis tools: AA; Wrote the manuscript: ZAR, AA.

Declaration of Interests

The authors declare no conflict of interest.

Figure legends

Figure titles and legends

Figure 1. Computational analysis deciphering the structural and interaction level insights of key host proteins, ACE2 (A to F), NRP-1 (G to J) and N501Y (K) involved in SARS-CoV-2 infection. (A) the sequence alignment of human and hamster ACE2 sequences. Along with secondary structure the residual variations are highlighted in yellow arrows indicating the differences among sequences. (B) crystal structure of human ACE2. The hACE2 (in blue), modelled haACE2 (in ice-blue), and RBD is in red. The surface view of h/ha ACE2 with RBD. (C) The residue level interaction map, ACE2, is rendered in cartoon and colored for h(blue) and for hamster (ice-blue). The amino acid residues are coloured as per atom-type such as O:red, N:blue, C:cyan/yellow/white. (D) The molecular docking data of ACE2 and RBD interaction (in Histogram). The selective docked pose is shown in a dotted rectangular box. (E and F) the interaction energies calculated at h/ha interfaces. The interacting residues are aromatic:purple, polar:green, acidic:red and aliphatic:grey. The types of interaction below $<-3.0 \text{ \AA}$ distance are shown by blue lines and hydrophobic interactions are in orange dotted lines. The bar graphs are the residue-wise interaction energies (in kcal/mol) for both RBD and ACE2. The key residues ($<-2.0 \text{ kcal/mol}$) are highlighted via green dotted lines. (G) The overlay of h/ha NRP-1 along with CendR peptide, rendered in cartoon. The zoom-out view of interacting interfaces of h/ha NRP-1 loop residues and CendR peptide residues. Peptide residues are rendered in licorice and color-coded in atom-wise. The hydrogen bond forming residues are shown by yellow lines. (H) the bar graph showing the residue-wise interaction energy. (I and J) the binding groove of NRP-1 showing how nicely CendR peptides fit in h/ha.

(K) The N501 and Y501 interaction patterns in hACE2-RBD. The bar graph showing the difference of 501 in h/ha in wild and mutant states.

Figure 2. Pulmonary pathologies of SARS-CoV2 infected hamsters. (A) % body mass change. (B) Gross morphology of lungs showing pneumonitis region. (C) Lung viral load expressed as Log10 copy number/g or log10 TCID50/g. (D) Microscopic images of HE and TB stained lungs (E) histological scores (F & G) lung qPCR showing mean relative mRNA expression with standard error mean (SEM). Alveolar epithelial injury (red), inflammation (blue), pneumonitis (yellow) and mast cells (black). *P < 0.05, **P < 0.01, ***P < 0.001, ****P < 0.0001 (one-way anova).

Figure 3. Immunological response against SARS-CoV2 infection in hamsters. (A) Changes in spleen length of SARS-CoV2 infected animals at different dpi as compared to uninfected animals (B) Serum IgG titre against SARS-CoV2 viral proteins (C) FACS for IFN γ secretion showing representative dot plots with % age frequency values and a bar graph showing mean \pm SEM. Relative mRNA expression of (D) cytokines, (E) transcription factors, (F) chemokines and (G) checkpoint inhibitors in the spleen of infected vs uninfected hamsters. *P < 0.05, **P < 0.01, ***P < 0.001, ****P < 0.0001 (one-way anova).

Figure 4. Cardiovascular complications in the heart of SARS-CoV2 infected hamsters. (A & B) heart HE stain captured at 1X and 10X showing ventricular walls and interstitial septum (green arrow) and inflammation around coronary artery (blue arrow) (B) heart MT stains showing interstitial coronary fibrosis (black arrow). (C) serum gross lipid profile. *P < 0.05, **P < 0.01, ***P < 0.001, ****P < 0.0001 (one-way anova).

Figure 5. Serum lipid profile of SARS-CoV2 infected hamster. (A) Scheme for lipidomics analysis (B) classification of detected lipid in this study (C) volcano plot for 2, 4, 7 and 14 dpi (D) Venn diagram for differentially regulated lipids (E & F) log2 fold change heatmap.

Figure 6. Serum metabolomics profile of SARS-CoV2 infected hamster. (A) Schematic representation for metabolomics. (B & C) Venn diagrams for differentially regulated. (D) volcano plot for 2, 4, 7 and 14 dpi. (E) heatmap for log2 fold change (F) pathways impacted. (G) Scheme and Venn diagram for correlation with Bo Shen et al 2020. (H) dot plot for relative abundance of metabolites common with severe profile (I) or severe vs non-severe profile. *P < 0.05 (one-way anova).

Star Methods

Animal Ethics and biosafety statement

6-8 weeks old female golden Syrian hamsters were acclimatized in biosafety level-2 (BSL-2) for one week and then infected in Animal BSL3 (ABSL-3) institutional facility. The animals were maintained under 12 h light and dark cycle and fed standard pellet diet and water ad libitum. All the experimental protocols involving the handling of virus culture and animal infection were approved by RCGM, institutional biosafety and IAEC animal ethics committee.

Virus preparation and determination of viral titers

SARS-Related Coronavirus 2, Isolate USA-WA1/2020 virus was used as challenge strain, which was grown and titrated in Vero E6 cell line grown in Dulbecco's Modified Eagle Medium (DMEM) complete media containing 4.5 g/L D-glucose, 100,000 U/L Penicillin-Streptomycin, 100 mg/L sodium pyruvate, 25mM HEPES and 2% FBS. The virus stocks were plaque purified and amplified at THSTI Infectious Disease Research Facility (Biosafety level 3 facility) as described previously (Harcourt et al., 2020; Mendoza et al., 2020).

SARS-CoV2 infection in golden Syrian hamster

Infection in golden Syrian hamsters were carried out as previously described (Chan et al., 2020; Sia et al., 2020). Briefly anesthetized through ketamine (150mg/kg) and xylazine (10mg/kg)

intraperitoneal injection and thereafter infection was established intranasally with 10^4 PFU (100µl) or 10^5 PFU (100µl) of live SARS-CoV2 or with DMEM mock control inside ABSL3 facility.

Clinical parameters of SARS-CoV2 infection

All infected animals were housed for 14 days and their body mass was monitored as previously described (Chan et al., 2020; Sia et al., 2020). 9 animals from each group were sacrificed on 2, 4, 7 and 14 days post infection (dpi) and their blood serum along with body organs such as lungs, intestine, liver, spleen and kidney were collected. Serum samples were stored at -80 °C until further use. Lung and spleen samples of infected and uninfected animals were compared for any gross morphological changes. Lungs samples were homogenized in 2 ml DMEM media and used for viral load and TCID50 determination. A section of lung, intestine along with other organs were fixed in 10% formalin solution and used for histological studies. Spleen were strained through 40 µm cell strainer with the help of syringe plunger and used for qPCR and immunophenotyping studies.

Viral load

Homogenized lung samples of 2, 4, 7, 14 dpi along with uninfected controls were centrifuged for 10 min at 4°C and their supernatant was collected. 100 µl of supernatant from each sample was then mixed with 900 µl of Trizol reagent (Invitrogen) and RNA isolation was carried out as per manufacturer's protocol. Copy number estimation of SARS-CoV-2 RNA has been described previously (Anantharaj et al., 2020). Briefly, 200 ng of RNA was used as template for reverse transcription polymerase chain reaction (RT-PCR). CDC-approved commercial kit was used for of SARS-CoV-2 N gene: 5'-GACCCCAAATCAGCGAAAT-3' (Forward), 5'-TCTGGTTACTGCCAGTTGAATCTG-3' (Reverse) and 5'-FAM-ACCCCGCATTACGTTTGGTGGACC-BHQ1 -3' (Probe) detection and sub-genomic RNA

copy numbers were estimated by $\Delta\Delta C_t$ method. Hypoxanthine-guanine phosphoribosyltransferase (HGPRT) gene was used as an endogenous control for normalization through quantitative RT-PCR. The region of N gene of SARS-CoV-2 starting from 28287 – 29230 was cloned into pGEM®-T-Easy vector (Promega). This clone was linearized using SacII enzyme and *in vitro* transcribed using the SP6 RNA polymerase (Promega). The transcript was purified and used as a template for generating standard curve to estimate the copy number of SARS-CoV-2 N RNA (Anantharaj et al., 2020).

TCID₅₀

For TCID₅₀ determination, 50 µl of homogenized lung supernatant samples were incubated with confluent Vero-E6 cells in 96-well plates as described previously (Chan et al., 2020). Briefly, serial dilutions of 10-folds from each sample were added to the wells containing Vero-E6 cells monolayer in DMEM media in quadruplicate. After 4 days of incubation, TCID₅₀ was determined through Reed and Munch endpoint method with one TCID₅₀ equivalent to the amount of virus required to cause cytopathic effect in 50% of inoculated wells. TCID₅₀ values were expressed as TCID₅₀/ gram of lung mass. For determination of virus titers, tissue samples (lungs) were homogenized to a final 10% (w/v) suspension in DMEM medium with gentamicin (Invitrogen, USA). The tissue samples from 2 to 14 dpi were used to infect Vero E6 cell monolayers in 48-plates as described previously. Virus titers were expressed as TCID₅₀ per gram of tissue

ELISA

The binding-antibody response to SARS CoV-2 post infection was measured using ELISA based platform as described earlier (Shrivastava et al., 2018). The antibody response was measured against Spike, RBD and N protein post virus challenge at different time point. Soluble spike prefusion trimeric protein (S2P) (Wrapp et al., 2020), in house RBD (Ha et al.,

2020) and N proteins were coated on Maxisorp plates (Nunc) at different protein concentrations (Spike S2P trimer; 1 µg/ml, RBD; 2µg/ml and N protein at 0.5ug/ml) in 1X carbonate/bicarbonate buffer, pH 9.6 overnight at 4 °C. The following day, the plates were blocked using 250 µl of PBS containing 5 % skimmed milk (blocking buffer). Three fold serially diluted sera (with 1:5 as starting dilution) in dilution buffer (1:5 times dilution of blocking buffer) were added to wells of the plates. The plates were incubated at room temperature (RT) for 1 h and then washed three times with washing buffer (PBS + 0.05 % tween 20), the ELISA plates with N protein coating were washed additionally once with high salt PBST (Phosphate buffer with 500 mM NaCl and 0.05 % Tween 20) and incubated with biotinylated anti-hamster IgG antibody (Sigma) for another 1 h and washed subsequently with the washing buffer and incubated further with Avidin-HRP (Sigma) for 45 min at RT. Post incubation plates were washed four times and 100 µl of TMB substrate (Thermo Fisher Scientific) was added to the washed wells. The reaction was stopped by adding 100 µl of 1 N H₂SO₄ and the plates were read at 450 nm on a 96-well microtiter plate reader. Sera end point titers were calculated as the reciprocal of serum dilution giving OD 450 nm readings higher than lowest dilution of the placebo or control arm + two times standard deviations

***In silico* molecular modelling and protein-protein docking**

In the absence of crystal structure of hamster ACE2 structures, the crystal structure of human ACE2 and RBD, pdb-ids 6m17, 6VW1 were considered as templates to generate the robust model of hamster through homology modelling (Srivastava et al., 2018). The robustness of each model was evaluated through ERRAT, PROSA and Ramachandran plot (allowed and disallowed %), followed by structure optimization through energy minimization to allow conformational relaxation of the protein structure (Ha et al., 2020). The same was carried out for neurolipin-1 protein of hamster as human neurolipin crystal structure (pdb-id 6JJQ) is reported. The most stable proteins were picked to perform the protein-protein (for RBD-ACE2)

and protein-peptide (NRP-1 and CendR peptide of spike protein) docking studies through different algorithms. Rigid docking through PyDock allows some steric clashes while flexible docking by SwarmDock was done on relaxed structures of proteins to generate candidate solutions with at least one near native structure (Mattapally et al., 2018). Clustering of docked poses was conducted to generate the most likely complex of ACE2-RBD and NRP1-Cend peptide based on number of conformers and lowest binding energy (from -50 to -40 kcal/mol). Post-docking analysis followed by energy minimization of complexes showed that both the protein structures displayed an initial structural rearrangement that was followed by convergence indicating structural fluctuation at interface site specially at residual level i.e conformational changes and chi angle variation. The overall structural fluctuation of hACE2 (human ACE2) was observed to be less than that of haACE2 (hamster ACE2). This is expected as the protein structure (template) of the former has high resolution and covers more space, while the latter is the model. An inventory of structural and energetic features of the complexes was obtained by analysing the hydrogen bonds (cut-off of 3.5Å for the donor-acceptor distance and 150° for the donor-hydrogen-acceptor angle) and hydrophobic contacts (non-polar atoms separated by a distance of at-most 4.0 Å). π - π interactions were considered to be formed when the short inter-atomic carbon-carbon distance (SICD) was smaller than 4.8 Å (Kanwal et al., 2016). In an effort to dissect these interactions from the docking simulations, total interaction energy between ACE2 and RBD was calculated, within the framework of Amber-force field description.

qPCR

RNA was isolated from lung homogenate and spleen samples using Trizol-choloroform as previously described (Rizvi et al., 2018). Thereafter, RNA was quantitated by NanoDrop and 1 µg of total RNA was then reverse-transcribed to cDNA using the iScript cDNA synthesis kit (Biorad; #1708891) (Roche). Diluted cDNAs (1:5) was used for qPCR by using KAPA

SYBR® FAST qPCR Master Mix (5X) Universal Kit (KK4600) on Fast 7500 Dx real-time PCR system (Applied Biosystems) and the results were analyzed with SDS2.1 software. The relative expression of each gene was expressed as fold change and was calculated by subtracting the cycling threshold (Ct) value of hypoxanthine-guanine phosphoribosyltransferase (HGPRT-endogenous control gene) from the Ct value of target gene (Δ CT). Fold change was then calculated according to the previously described formula $POWER(2, -\Delta CT) \times 10,000$ (Malik et al., 2017). The list of the primers are provided as follows.

Gene	Forward	Reverse
HGPRT	GATAGATCCACTCCCATAACTG	TACCTTCAACAATCAAGACATTC
Rorc	GGGAAATGTGGGAACGCTGT	AAACGCAAGGCACTGAGGAA
tryptase beta-2	TCGCCACTGTATCCCCTGAA	CTAGGCACCCTTGACTTTGC
chymase	ATGAACCACCCTCGGACACT	AGAAGGGGGGCTTTGCATTCC
muc1	CGGAAGAACTATGGGCAGCT	GCCACTACTGGGTTGGTGTAAG
Foxo1	AGGATAAGGGCGACAGCAAC	GTCCCCGGCTCTTAGCAAAT
Sftpd	TGAGCATGACAGACGTGGAC	GGCTTAGAACTCGCAGACGA
Eotaxin	ATGTGCTCTCAGGTCATCGC	TCCTCAGTTGTCCCCATCCT
Ager	ATTCCTGACGGCAAAGGGAC	ACTGTGTTTCGAGGGACTGTG
PAI-1	CCGTGGAACCAGAACGAGAT	ACCAGAATGAGGCGTGTGTCAG
IFN γ	TGTTGCTCTGCCTCACTCAGG	AAGACGAGGTCCCCCTCCATTC
TNF α	AGAATCCGGGCAGGTCTACT	TATCCCGGCAGCTTGTGTTT
IL13	AAATGGCGGGTTCTGTGC	AATATCCTCTGGGTCTTGTAGATGG
IL17A	ATGTCCAAACACTGAGGCCAA	GCGAAGTGGATCTGTTGAGGT
IL9	CTCTGCCCTGCTCTTTGGTT	CGAGGGTGGGTCAATTCTTCA
TGF β	ACGGAGAAGAAGTGTGTG	GGTTGTGTTGGTTGTAGAGG
IL10	GGTTGCCAAACCTTATCAGAA ATG	TTCACCTGTTCCACAGCCTTG
T-bet	ACAAGGGGGCTTCCAACAAT	CAGCTGAGTGATCTCGGCAT
GATA3	GAAGGCAGGGAGTGTGTGAA	GTC TGA CAG TTC GCA CAG GA
FOXP3	GGTCTTCGAGGAGCCAGAAGA	GCCTTGCCC TTC TCA TCC A
CCR5	TGT GAC ATC CGT TCC CCC T	GGC AGG GTG CTG ACA TAC TA
CCL5	CTACGCTCCTTCATC TGC CTC	CCT TCG GGT GAC AAA AAC GAC
CCL22	CGT GGC TCT CAT CCT TCT TGC	CAG ATG CTG TCT TCC ACG TTG G
CXCL9	TGG GTA TCA TCC TCC TGG AC	AAT GAG GAC CTG GAG CAA AC
CXCL10	TGGAAATTATTCCTGCAAGTCA	GTG ATC GGC TTC TCT CTG GT
PD1	CTGAAAAGGGTTAAG CCA GC	GCC TCC AGG ATT CTC TCT GTT
PDL1	TGATCATCCCAGACCCGCTC	CTC CTC GAA CTG CGT ATC GT
IL6	GGACAATGACTATGTGTTGTTAGAA	AGGCAAATTTCCCAATTGTATCCAG
iNOS	TGAGCCACTGAGTTCTCCTAAGG	TCCTATTTCAACTCCAAGATGTTCTG

Histology

Excised tissues of animal organs were fixed in 10% formaline solution and processed for paraffin embedding. The paraffin blocks were cut into 3- μ m-thick sections and then mounted on silane-coated glass slides. One section from each organ samples was stained with hematoxylin and eosin. Lung, heart and colon samples were stained with taulidine blue, masson's trichrome and mucicarmine stains respectively. Each stained section was analysed and captured at 10X and 60X magnification. Heart images were also captured at 1X magnification. Blind assessment and scoring of each section for each samples was performed by professional histologist.

Immunophenotyping of splenocytes

0.5 million RBC lysed splenocytes were used for intracellular cytokine staining by re-stimulation with PMA (phorbol 12-myristate13-acetate; 50 ng/ml; Sigma-Aldrich), ionomycin (1.0 μ g/ml; Sigma-Aldrich) and monensin (#554724; GolgiStop, BD Biosciences) for 6 h or with RBD protein (50 μ g) for 72 h. Cell surface staining with anti-mouse CD4 (GK1.5) PerCp (Biolegend) was carried out for 20 min in dark at RT. Intracellular anti-mouse IFN- γ (XMG1.2) (BioLegend) staining was then carried out after fixing the cells in Cytofix solution and permeabilization with 1X Perm/Wash Buffer using kit (BD Biosciences; #554714) for 20 min in dark at RT. Cells were then washed and acquired on FACS Canto II and were analysed with FlowJo software (Tree star) as previously described (Malik et al., 2017).

Lipid extraction and lipidomics

Lipid extraction from serum sample was performed as previously described method with some modifications (Schwaiger et al., 2018). 0.3 ml methanol was added to 100 μ l of serum samples and mixed for 30 sec followed by addition of 1.25 ml methyl-tert-butyl ether (MTBE). The mixture was incubated at RT for 1 h on a shaker followed by addition of 0.3 ml of MS grade water was for the phase separation. 10 min after incubation at RT, samples were spin down at

400 rpm at 10 °C for 5 min. Organic upper phase was collected and dried in a speed vac and stored at -80 °C till further use. Moreover, lipids extracted were dissolved in 100 µl of 65:30:5 (acetonitrile: 2-propanol: water v/v/v). An acquity HSS T3 (2.1 mm X 100 mm X 1.8 µm, WATERS) was then utilized for carrying out lipid separation by exploiting ultra-performance liquid chromatography (UPLC). Solvent A and B were water/ acetonitrile (2:3 v/v) and 2-propanol/acetonitrile (9:1, v/v) respectively, at 0.3ml/min flow rate and 40 °C column temperature. 18 min total run time was utilized with the following gradient setup, 0 to 12 min solvent B ramped from 30 to 97% and a hold for another 3 min. From 15.2 to 18 min, B was at 30%. Acquisition of data was carried out on a high-resolution mass spectrometer, orbitrap fusion (Thermo Scientific) equipped with a heated electrospray ionization source. Auxiliary gas and ESI sheath gas were 20 and 60 respectively. Negative and positive spray voltage was 3000 volts. For full MS run, 120k resolution was used with automatic gain control (AGC) targeted of 200000 and mass ranges between 250-1200. Resolution was kept at 30K with AGC target 50000 for MSMS. Collision energy for fragmentation used was 27+/-3.

Lipid data analysis

Lipidmatch flow was utilized with default settings for peak picking (using mzmne), lipid annotation, blank filtration and combining positive and negative data (Koelmel et al., 2017). Thereafter, data analysis was carried out as follows: the data was normalized by sum, perato scaled, and log-transformed for analysis in metaboanalyst.

Metabolomics analysis LC-MS/MS reverse phase and HILIC

Metabolites were extracted from 100 µl of serum samples by using 100% methanol. Thereafter, mixture were vortexed for 1 min and kept on ice for protein precipitation. After centrifugation (10000 rpm for 10 min at 4 °C) supernatant was collected and distributed in two tubes for polar and nonpolar metabolite analysis. Collected supernatants were then dried using a speed vacuum

at for 20 to 25 min at RT and stored at -80 °C till further analysis. For reverse phase metabolites were dissolved in 15% methanol in water (v/v) and for polar metabolite analysis samples were dissolved in 50% acetonitrile in water (v/v).

Measurement of metabolites

Orbitrap Fusion mass spectrometer (Thermo Scientific) coupled with heated electrospray ion source was used for data acquisition. Data acquisition methods have been followed as per published protocols (Kumar et al., 2020; Naz et al., 2017) with minor modifications. Briefly for MS1 mode, mass resolution was kept at 120,000 and for MS2 acquisition, mass resolution was 30,000. Mass range of data acquisition was 60–900 da. Extracted metabolites were separated on UPLC ultimate 3,000. Data were acquired on reverse phase and HILIC column and positive and negative ionization mode both. Reverse phase column was HSS T3 and HILIC column was XBridge BEH Amide (Waters Corporation). For polar compound separation, solvent A was 20 mM ammonium acetate in the water of PH 9.0 and mobile phase B was 100% acetonitrile. The elution gradient starts from 85% B to 10% B over 14 min with flow rate of 0.35 ml/min. For reverse phase, Solvent A was water and B was methanol with 0.1% formic acids added in both. The elution gradient starts with 1% B to 95% B over 10 min with flow rate 0.3 ml/min. sample injection volume was 5ul. Pool quality control (QC) sample was run after every five samples to monitor signal variation and drift in mass error. Data matrices have been provided in Supplementary Table 1 and representative spectra of one of the samples acquired in positive and negative modes of HILIC and RP have been provided in Supplementary Fig. 3. Data processing. All LC/MS acquired data has been processed using the Progenesis QI for metabolomics (Water Corporation) software using the default setting. The untargeted workflow of Progenesis QI was used to perform retention time alignment, feature detection, deconvolution, and elemental composition prediction. Metascope plug of Progenesis QI has been used for the in-house library with accurate mass, fragmentation pattern and retention time

for database search. We have also used online available spectral library for further confirmation of identification. Cut-off for retention time match was 0.5 min and spectral similarity was more than 30% fragmentation match in Progenesis QI. Peaks that had a coefficient of variation (CV) less than 30% in pool QC samples were kept for the further analysis of data. Additionally, manual verification of each detected feature has been done for the selection of right peaks.

Lipidomics and metabolomics data analysis

For both metabolomics and lipidomics data, the data was cleaned up to remove zero intensity values. The average calculations were done with the remaining available intensity values. The fold change was calculated as the ratio of average intensity values of cases divided by the average intensity of controls as-

$$FC = \frac{\frac{(\sum_{i=1}^m I_{ki})}{m}}{\frac{(\sum_{j=1}^n I_j)}{n}}$$

Where,

FC = fold change

m = number of available non-zero intensity values for case

n = number of available non-zero intensity values for control

I_{ki} = intensity of i^{th} case sample for condition k , where $k \in \{2D, 4D, 7D, 14D \text{ post infection}\}$

I_j = intensity of j^{th} control sample

A two-tailed t-test considering similar means of case and control population was used to calculate the p-values. The FC was transformed to $\log_2 FC$ and a threshold was set to ± 2 FC (± 1 at $\log_2 FC$). The significance threshold for differential expression was set using simultaneous threshold filters of the $\log_2 FC$ of ± 1 as well as a p-value threshold of ≤ 0.05 . This was followed for both the metabolomics and the lipidomics data. The significantly expressed analytes (metabolites and the lipids) are also represented on the volcano plots. For the volcano plots,

the p-values were transformed into $-\log_{10}$ P-values for plotting. The significant values as described above were highlighted and labeled on the graph using Tableau (version 2020.3).

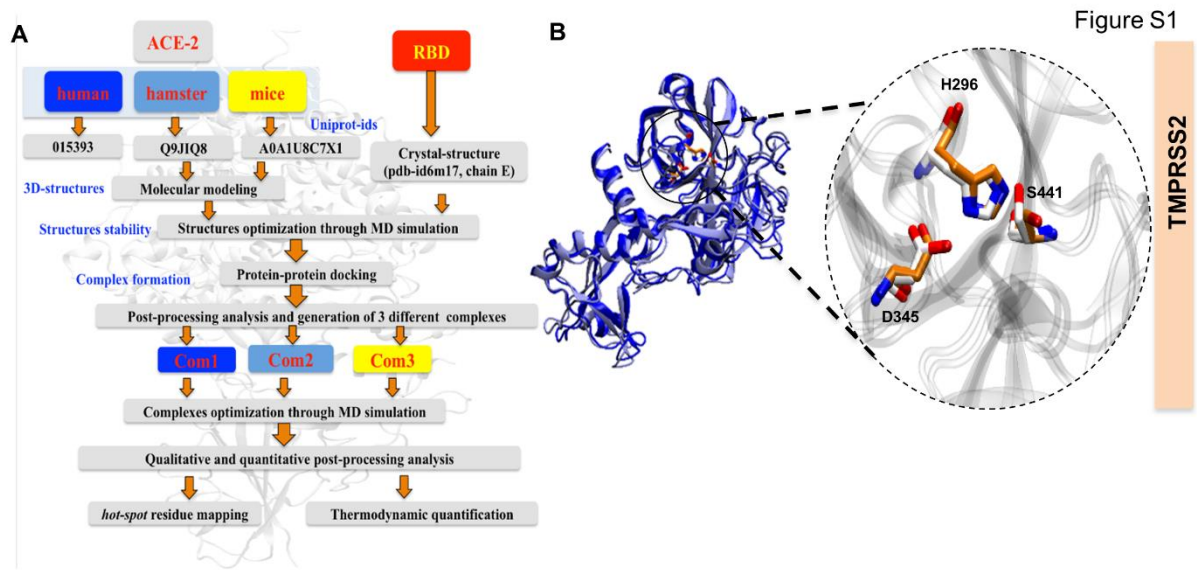
Volcano plot $-\log_{10}$ P value vs \log_2 fold change was plotted on the Volcano plot. Tableau (version 2020.3) was used to highlight and annotate some of the significant hits (metabolites/lipids). The points above or below $\pm 1 \log_2$ fold change (i.e. ± 2 fold change) and 1.33 on the $-\log_{10}$ Pvalue scale (i.e. ≤ 0.05 p-value) were selected for annotation and were colored red for visual distinction. For the heat map construction, we used \log_2 fold changes for both the metabolites as well as lipids heat maps. Gene-E software (<https://software.broadinstitute.org/GENE-E/>) was used to create the heat maps. For the analyte (metabolite/lipid) with a zero values in control but a positive intensity reading value in cases, we considered them as overexpressed vs control in that particular condition, and used a maximum \log_2 FC imputed manually. The value chosen for such cases was the maximum value from the data. For setting the color scale, we used blue color to represent all the values below $-4 \log_2$ FC (1/16 FC) and all the values above $+4 \log_2$ FC were colored red (+16 FC). **For whole data heat map** Clustvis was used to generate the heat map for the complete dataset for both metabolites as well as lipids. **PCA plots** raw values of the metabolites and lipids were taken for all 9 samples. The web-based tool ClustVis was used to create the sample PCA plots to check the clustering of biological samples (ClustVis: a web tool for visualizing clustering of multivariate data using Principal Component Analysis and heatmap) (Metsalu and Vilo, 2015).

Comparison against the human data The data from the article (Shen et al., 2020) was downloaded and manually compared with the hamster metabolites data obtained from our study. The metabolites common to each category were then compared against each other to identify metabolites unique to each category as classified by the authors.

Statistical analysis

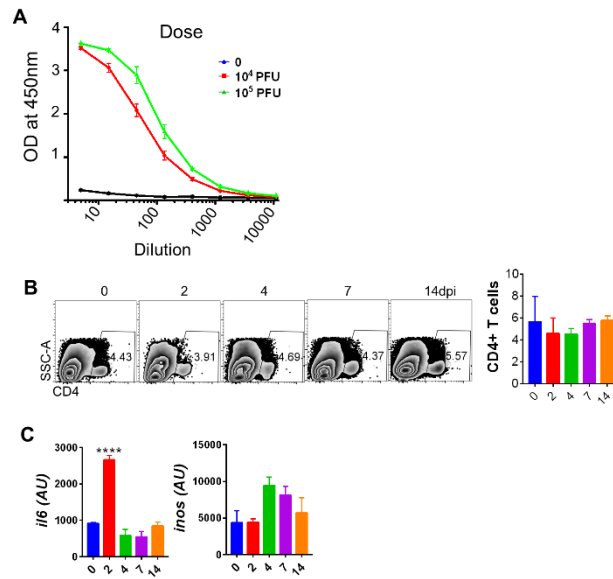
All the results were analysed and plotted by using Graph pad prism 7.0 software. Body mass, lung mass, gene expression, FACS, ELISA, TCID₅₀ and qPCR studies were compared and analyzed by using one-way ANOVA or student t-test for n = 6 hamsters samples per group. Metabolomics and lipidomics analysis was carried out with n=9 serum samples per group. P-value of less than 0.05 and was considered as statistically significant.

Supplementary figures



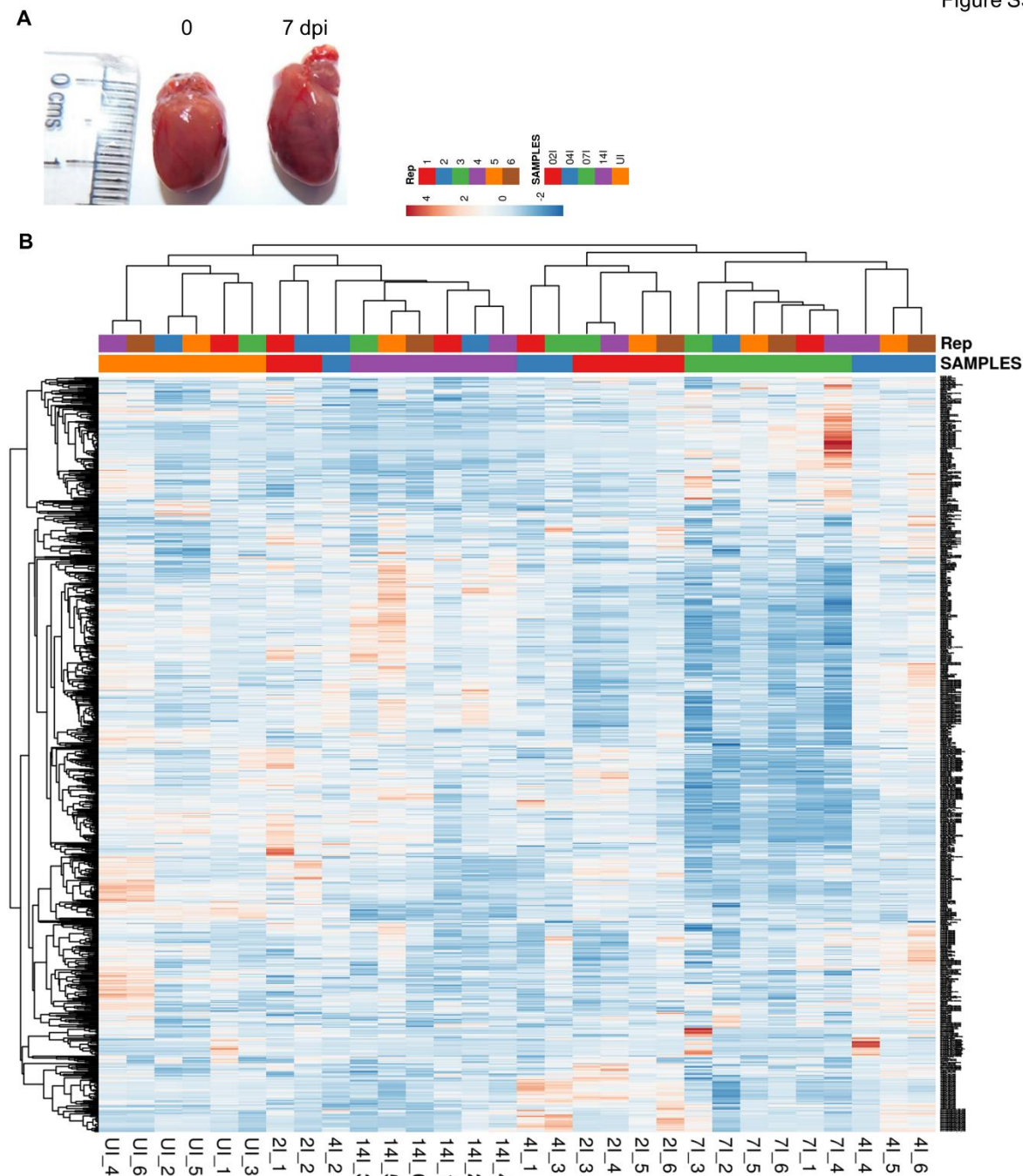
Supplementary figure 1. *In silico* analysis. (A) Scheme for h/ha ACE2-RBD interaction (B) catalytic triad for hamster TMPRSS2.

Figure S2



Supplementary figure 2. Immunological response. (A) antibody titre for different dose of infection (B) FACS dot plot and bar graph showing mean \pm SEM % frequency of CD4+ cells. (C) bar graph showing mean value \pm SEM of mRNA expression of IL6 and iNOS genes in the splenocytes samples. ****P < 0.0001 (one-way anova).

Figure S3



Supplementary figure 3. Morphological changes in heart and lipid relative abundance heatmap. (A) Heart hypertrophy on 7 dpi (B) heatmap for normalized relative abundance.

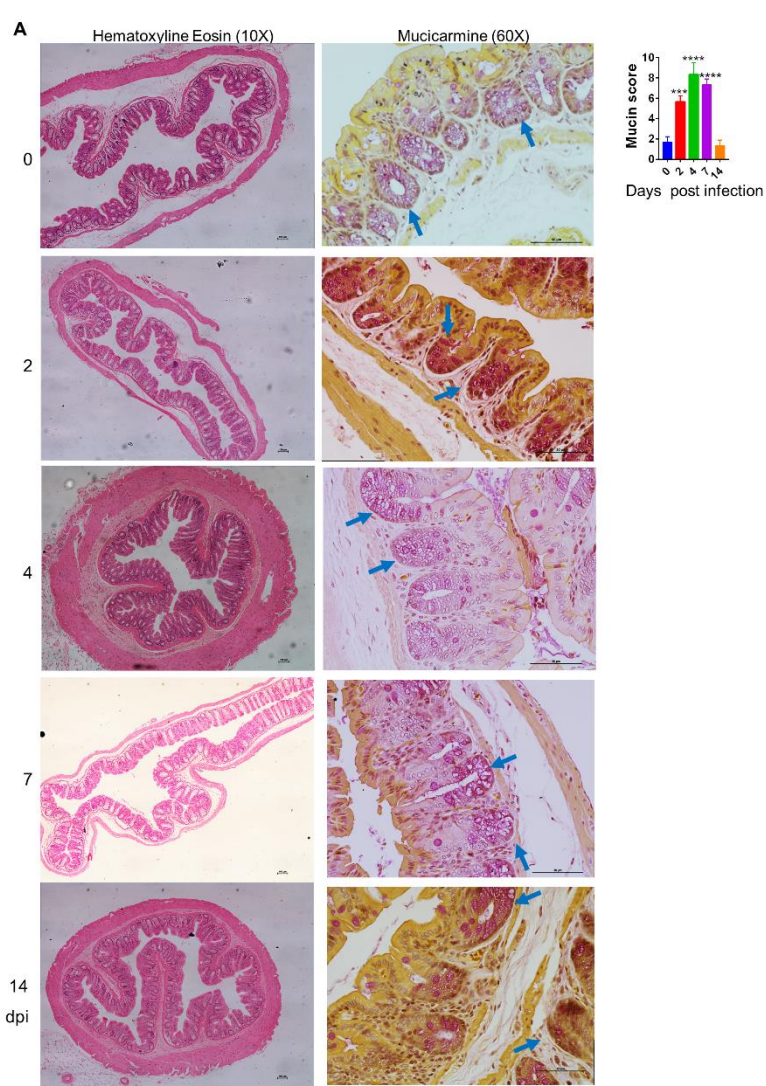
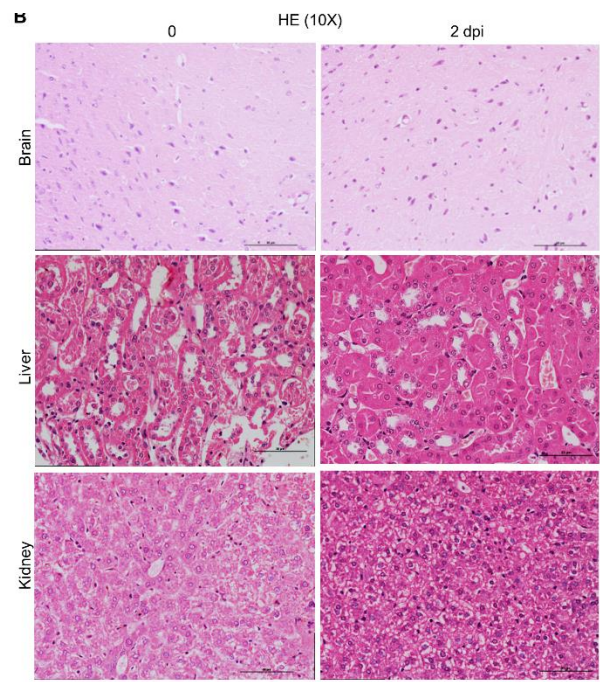
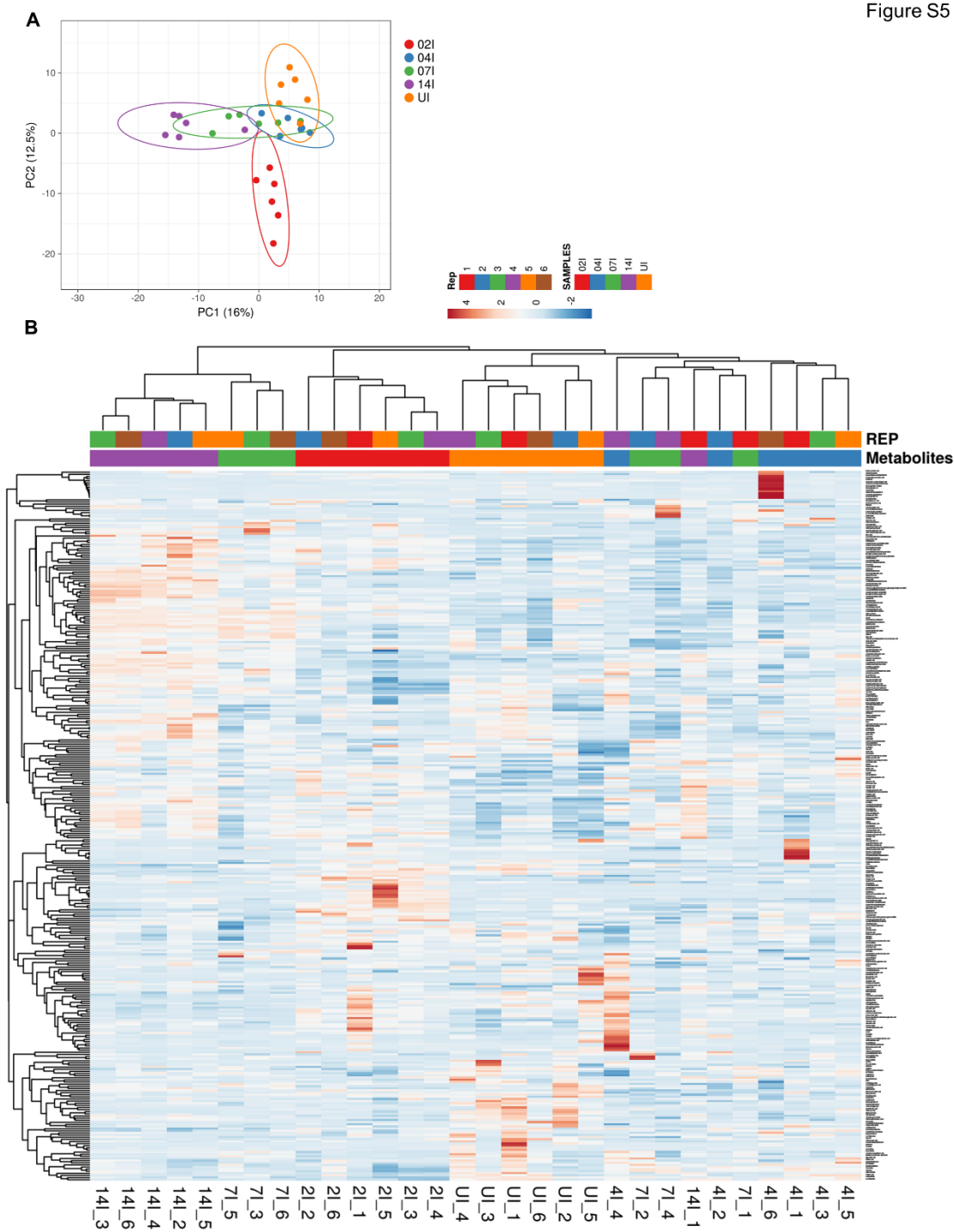


Figure S4



723 **Supplementary figure 4. Extra-pulmonary changes** (A) H & E stain (B) mucicarmin stain
 724 for the presence of mucin (blue arrow) of colon on 2, 4, 7 and 14 dpi (C) H & E stain for brain,
 725 liver and kidney on 2 dpi. ***P < 0.001, ****P < 0.0001 (one-way anova).

Figure S5



726

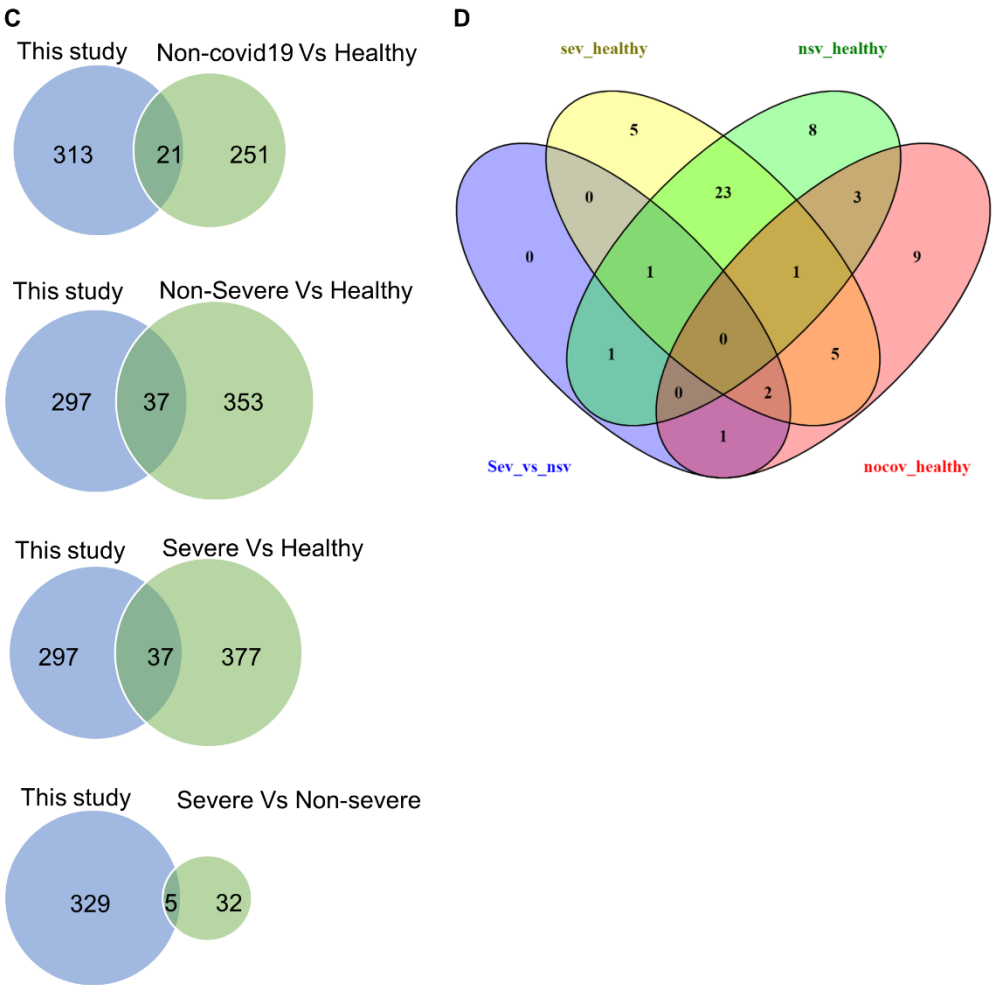


Figure S5

Supplementary figure 5. Metabolomics. (A) PCA plot for metabolomics (B) heatmap showing normalized relative abundance (C & D) Venn diagram showing correlation of metabolites with Bo Shen et. al. metabolomics profile in covid19 patients.

References

- Afrin, L.B., Weinstock, L.B., and Molderings, G.J. (2020). Covid-19 hyperinflammation and post-Covid-19 illness may be rooted in mast cell activation syndrome. *International Journal of Infectious Diseases* 100, 327–332.
- Anantharaj, A., Gujjar, S., Kumar, S., Verma, N., Wangchuk, J., Khan, N.A., Panwar, A., Kanakan, A., A, V., Vasudevan, J.S., et al. (2020). Kinetics of viral load, immunological mediators and characterization of a SARS-CoV-2 isolate in mild COVID-19 patients during acute phase of infection. *MedRxiv* 2020.11.05.20226621.
- Cantuti-Castelvetri, L., Ojha, R., Pedro, L.D., Djannatian, M., Franz, J., Kuivanen, S., Meer, F. van der, Kallio, K., Kaya, T., Anastasina, M., et al. (2020). Neuropilin-1 facilitates SARS-CoV-2 cell entry and infectivity. *Science* 370, 856–860.

742 Chan, J.F.-W., Zhang, A.J., Yuan, S., Poon, V.K.-M., Chan, C.C.-S., Lee, A.C.-Y., Chan,
743 W.-M., Fan, Z., Tsoi, H.-W., Wen, L., et al. (2020). Simulation of the Clinical and
744 Pathological Manifestations of Coronavirus Disease 2019 (COVID-19) in a Golden Syrian
745 Hamster Model: Implications for Disease Pathogenesis and Transmissibility. *Clinical*
746 *Infectious Diseases* 71, 2428–2446.

747 Chen, Y., and Li, L. (2020). SARS-CoV-2: virus dynamics and host response. *The Lancet*
748 *Infectious Diseases* 20, 515–516.

749 Daly, J.L., Simonetti, B., Klein, K., Chen, K.-E., Williamson, M.K., Antón-Plágaro, C.,
750 Shoemark, D.K., Simón-Gracia, L., Bauer, M., Hollandi, R., et al. (2020). Neuropilin-1 is a
751 host factor for SARS-CoV-2 infection. *Science* 370, 861–865.

752 Giustino, G., Pinney, S.P., Lala, A., Reddy, V.Y., Johnston-Cox, H.A., Mechanick, J.I.,
753 Halperin, J.L., and Fuster, V. (2020). Coronavirus and Cardiovascular Disease, Myocardial
754 Injury, and Arrhythmia. *J Am Coll Cardiol* 76, 2011–2023.

755 Grifoni, A., Weiskopf, D., Ramirez, S.I., Mateus, J., Dan, J.M., Moderbacher, C.R.,
756 Rawlings, S.A., Sutherland, A., Premkumar, L., Jadi, R.S., et al. (2020). Targets of T Cell
757 Responses to SARS-CoV-2 Coronavirus in Humans with COVID-19 Disease and Unexposed
758 Individuals. *Cell* 181, 1489-1501.e15.

759 Ha, P., Ak, C., S, A., N, Y., T, S., S, M., C, S., P, V., S, D., K, P., et al. (2020). Identification
760 of an anti-SARS-CoV-2 receptor-binding domain-directed human monoclonal antibody from
761 a naïve semisynthetic library. *J Biol Chem* 295, 12814–12821.

762 Harcourt, J., Tamin, A., Lu, X., Kamili, S., Sakthivel, S.Kumar., Murray, J., Queen, K., Tao,
763 Y., Paden, C.R., Zhang, J., et al. (2020). Isolation and characterization of SARS-CoV-2 from
764 the first US COVID-19 patient. *BioRxiv*.

765 Hoffmann, M., Kleine-Weber, H., Schroeder, S., Krüger, N., Herrler, T., Erichsen, S.,
766 Schiergens, T.S., Herrler, G., Wu, N.-H., Nitsche, A., et al. (2020). SARS-CoV-2 Cell Entry
767 Depends on ACE2 and TMPRSS2 and Is Blocked by a Clinically Proven Protease Inhibitor.
768 *Cell* 181, 271-280.e8.

769 Imai, M., Iwatsuki-Horimoto, K., Hatta, M., Loeber, S., Halfmann, P.J., Nakajima, N.,
770 Watanabe, T., Ujie, M., Takahashi, K., Ito, M., et al. (2020). Syrian hamsters as a small
771 animal model for SARS-CoV-2 infection and countermeasure development. *Proceedings of*
772 *the National Academy of Sciences* 202009799.

773 Kanwal, A., Kasetti, S., Putcha, U.K., Asthana, S., and Banerjee, S.K. (2016). Protein kinase
774 C-mediated sodium glucose transporter 1 activation in precondition-induced cardioprotection.
775 *Drug Des Devel Ther* 10, 2929–2938.

776 Koelmel, J.P., Kroeger, N.M., Ulmer, C.Z., Bowden, J.A., Patterson, R.E., Cochran, J.A.,
777 Beecher, C.W.W., Garrett, T.J., and Yost, R.A. (2017). LipidMatch: an automated workflow
778 for rule-based lipid identification using untargeted high-resolution tandem mass spectrometry
779 data. *BMC Bioinformatics* 18, 331.

780 Kong, P., Christia, P., and Frangogiannis, N.G. (2014). The Pathogenesis of Cardiac Fibrosis.
781 *Cell Mol Life Sci* 71, 549–574.

782 Kumar, A., Kumar, Y., Sevak, J.K., Kumar, S., Kumar, N., and Gopinath, S.D. (2020).
783 Metabolomic analysis of primary human skeletal muscle cells during myogenic progression.
784 Scientific Reports 10, 11824.

785 Labarthe, F., Gélinas, R., and Des Rosiers, C. (2008). Medium-chain Fatty Acids as
786 Metabolic Therapy in Cardiac Disease. Cardiovasc Drugs Ther 22, 97–106.

787 Lamers, M.M., Beumer, J., Vaart, J. van der, Knoop, K., Puschhof, J., Breugem, T.I.,
788 Ravelli, R.B.G., Schayck, J.P. van, Mykytyn, A.Z., Duimel, H.Q., et al. (2020). SARS-CoV-2
789 productively infects human gut enterocytes. Science 369, 50–54.

790 Lee, A.C.-Y., Zhang, A.J., Chan, J.F.-W., Li, C., Fan, Z., Liu, F., Chen, Y., Liang, R.,
791 Sridhar, S., Cai, J.-P., et al. (2020). Oral SARS-CoV-2 Inoculation Establishes Subclinical
792 Respiratory Infection with Virus Shedding in Golden Syrian Hamsters. Cell Reports
793 Medicine 1, 100121.

794 Malik, S., Sadhu, S., Elesela, S., Pandey, R.P., Chawla, A.S., Sharma, D., Panda, L., Rathore,
795 D., Ghosh, B., Ahuja, V., et al. (2017). Transcription factor Foxo1 is essential for IL-9
796 induction in T helper cells. Nat Commun 8, 815.

797 Mao, L., Jin, H., Wang, M., Hu, Y., Chen, S., He, Q., Chang, J., Hong, C., Zhou, Y., Wang,
798 D., et al. (2020). Neurologic Manifestations of Hospitalized Patients With Coronavirus
799 Disease 2019 in Wuhan, China. JAMA Neurol 77, 683–690.

800 Mathew, D., Giles, J.R., Baxter, A.E., Oldridge, D.A., Greenplate, A.R., Wu, J.E., Alanio, C.,
801 Kuri-Cervantes, L., Pampena, M.B., D’Andrea, K., et al. (2020). Deep immune profiling of
802 COVID-19 patients reveals distinct immunotypes with therapeutic implications. Science 369.

803 Mattapally, S., Singh, M., Murthy, K.S., Asthana, S., and Banerjee, S.K. (2018).
804 Computational modeling suggests impaired interactions between NKX2.5 and GATA4 in
805 individuals carrying a novel pathogenic D16N NKX2.5 mutation. Oncotarget 9, 13713–
806 13732.

807 Mendoza, E.J., Manguiat, K., Wood, H., and Drebot, M. (2020). Two Detailed Plaque Assay
808 Protocols for the Quantification of Infectious SARS-CoV-2. Curr Protoc Microbiol 57,
809 ecpmc105.

810 Metsalu, T., and Vilo, J. (2015). ClustVis: a web tool for visualizing clustering of
811 multivariate data using Principal Component Analysis and heatmap. Nucleic Acids Res 43,
812 W566–570.

813 Moore, J.B., and June, C.H. (2020). Cytokine release syndrome in severe COVID-19.
814 Science 368, 473–474.

815 Naz, S., Gallart-Ayala, H., Reinke, S.N., Mathon, C., Blankley, R., Chaleckis, R., and
816 Wheelock, C.E. (2017). Development of a Liquid Chromatography–High Resolution Mass
817 Spectrometry Metabolomics Method with High Specificity for Metabolite Identification
818 Using All Ion Fragmentation Acquisition. Anal. Chem. 89, 7933–7942.

819 Nishiga, M., Wang, D.W., Han, Y., Lewis, D.B., and Wu, J.C. (2020). COVID-19 and
820 cardiovascular disease: from basic mechanisms to clinical perspectives. Nature Reviews
821 Cardiology 17, 543–558.

822 Rizvi, Z.A., Puri, N., and Saxena, R.K. (2018). Evidence of CD1d pathway of lipid antigen
823 presentation in mouse primary lung epithelial cells and its up-regulation upon
824 *Mycobacterium bovis* BCG infection. *PLOS ONE* 13, e0210116.

825 Schwaiger, M., Schoeny, H., Abiead, Y.E., Hermann, G., Rampler, E., and Koellensperger,
826 G. (2018). Merging metabolomics and lipidomics into one analytical run. *Analyst* 144, 220–
827 229.

828 Shen, B., Yi, X., Sun, Y., Bi, X., Du, J., Zhang, C., Quan, S., Zhang, F., Sun, R., Qian, L., et
829 al. (2020). Proteomic and Metabolomic Characterization of COVID-19 Patient Sera. *Cell*
830 182, 59-72.e15.

831 Shrivastava, T., Samal, S., Tyagi, A.K., Goswami, S., Kumar, N., Ozorowski, G., Ward,
832 A.B., and Chakrabarti, B.K. (2018). Envelope proteins of two HIV-1 clades induced different
833 epitope-specific antibody response. *Vaccine* 36, 1627–1636.

834 Sia, S.F., Yan, L.-M., Chin, A.W.H., Fung, K., Choy, K.-T., Wong, A.Y.L., Kaewpreedee, P.,
835 Perera, R.A.P.M., Poon, L.L.M., Nicholls, J.M., et al. (2020). Pathogenesis and transmission
836 of SARS-CoV-2 in golden hamsters. *Nature* 583, 834–838.

837 Srivastava, M., Suri, C., Singh, M., Mathur, R., and Asthana, S. (2018). Molecular dynamics
838 simulation reveals the possible druggable hot-spots of USP7. *Oncotarget* 9, 34289–34305.

839 Sungnak, W., Huang, N., Bécavin, C., Berg, M., Queen, R., Litvinukova, M., Talavera-
840 López, C., Maatz, H., Reichart, D., Sampaziotis, F., et al. (2020). SARS-CoV-2 entry factors
841 are highly expressed in nasal epithelial cells together with innate immune genes. *Nature*
842 *Medicine* 26, 681–687.

843 Travers, J.G., Kamal, F.A., Robbins, J., Yutzey, K.E., and Blaxall, B.C. (2016). Cardiac
844 Fibrosis: The Fibroblast Awakens. *Circ Res* 118, 1021–1040.

845 Verity, R., Okell, L.C., Dorigatti, I., Winskill, P., Whittaker, C., Imai, N., Cuomo-
846 Dannenburg, G., Thompson, H., Walker, P.G.T., Fu, H., et al. (2020). Estimates of the
847 severity of coronavirus disease 2019: a model-based analysis. *Lancet Infect Dis* 20, 669–677.

848 Wang, T., Du, Z., Zhu, F., Cao, Z., An, Y., Gao, Y., and Jiang, B. (2020). Comorbidities and
849 multi-organ injuries in the treatment of COVID-19. *The Lancet* 395, e52.

850 Wrapp, D., Wang, N., Corbett, K.S., Goldsmith, J.A., Hsieh, C.-L., Abiona, O., Graham,
851 B.S., and McLellan, J.S. (2020). Cryo-EM structure of the 2019-nCoV spike in the prefusion
852 conformation. *Science* 367, 1260–1263.

853 Wu, Y., Xu, X., Chen, Z., Duan, J., Hashimoto, K., Yang, L., Liu, C., and Yang, C. (2020).
854 Nervous system involvement after infection with COVID-19 and other coronaviruses. *Brain*
855 *Behav Immun* 87, 18–22.

856 Xiao, F., Tang, M., Zheng, X., Liu, Y., Li, X., and Shan, H. (2020). Evidence for
857 Gastrointestinal Infection of SARS-CoV-2. *Gastroenterology* 158, 1831-1833.e3.

858 Xydakis, M.S., Dehgani-Mobaraki, P., Holbrook, E.H., Geisthoff, U.W., Bauer, C.,
859 Hautefort, C., Herman, P., Manley, G.T., Lyon, D.M., and Hopkins, C. (2020). Smell and
860 taste dysfunction in patients with COVID-19. *Lancet Infect Dis* 20, 1015–1016.

Zhang Lei, Wei Ting-Ting, Li Yong, Li Jing, Fan Yong, Huang Feng-Qing, Cai Yuan-Yuan,
Ma Gaoxiang, Liu Jin-Feng, Chen Qian-Qian, et al. (2018). Functional Metabolomics
Characterizes a Key Role for N-Acetylneuraminic Acid in Coronary Artery Diseases.
Circulation 137, 1374–1390.

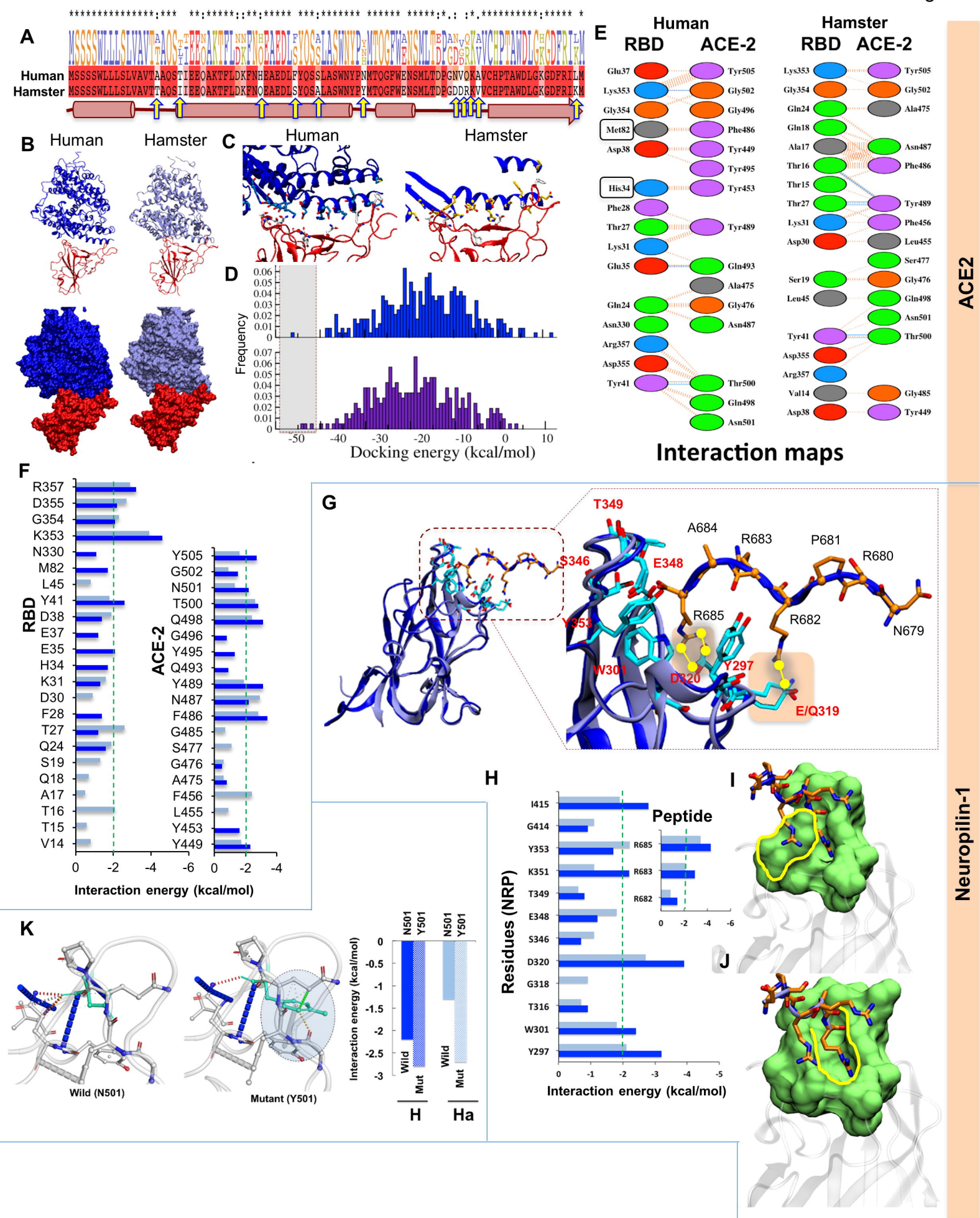


Figure 2

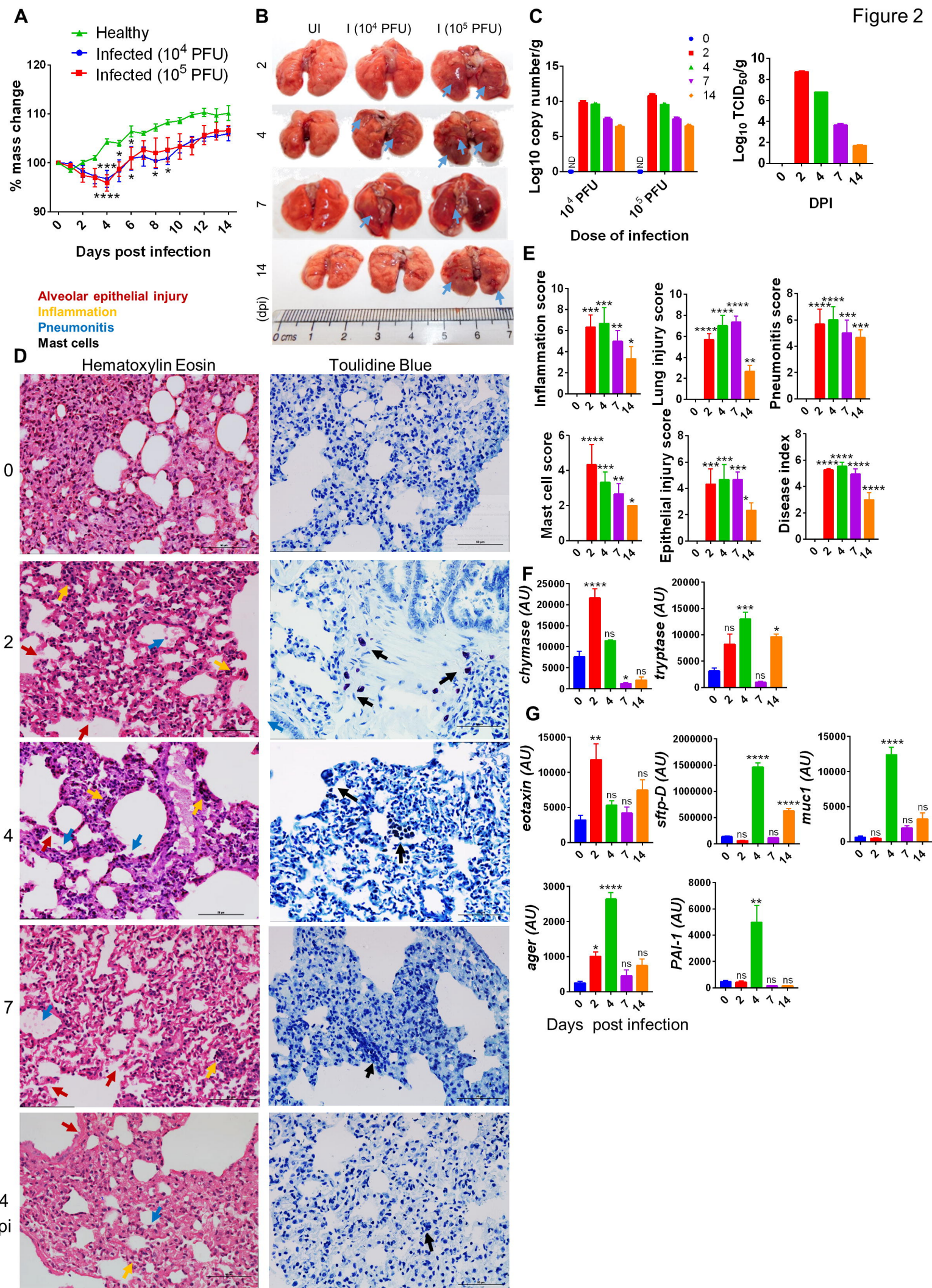
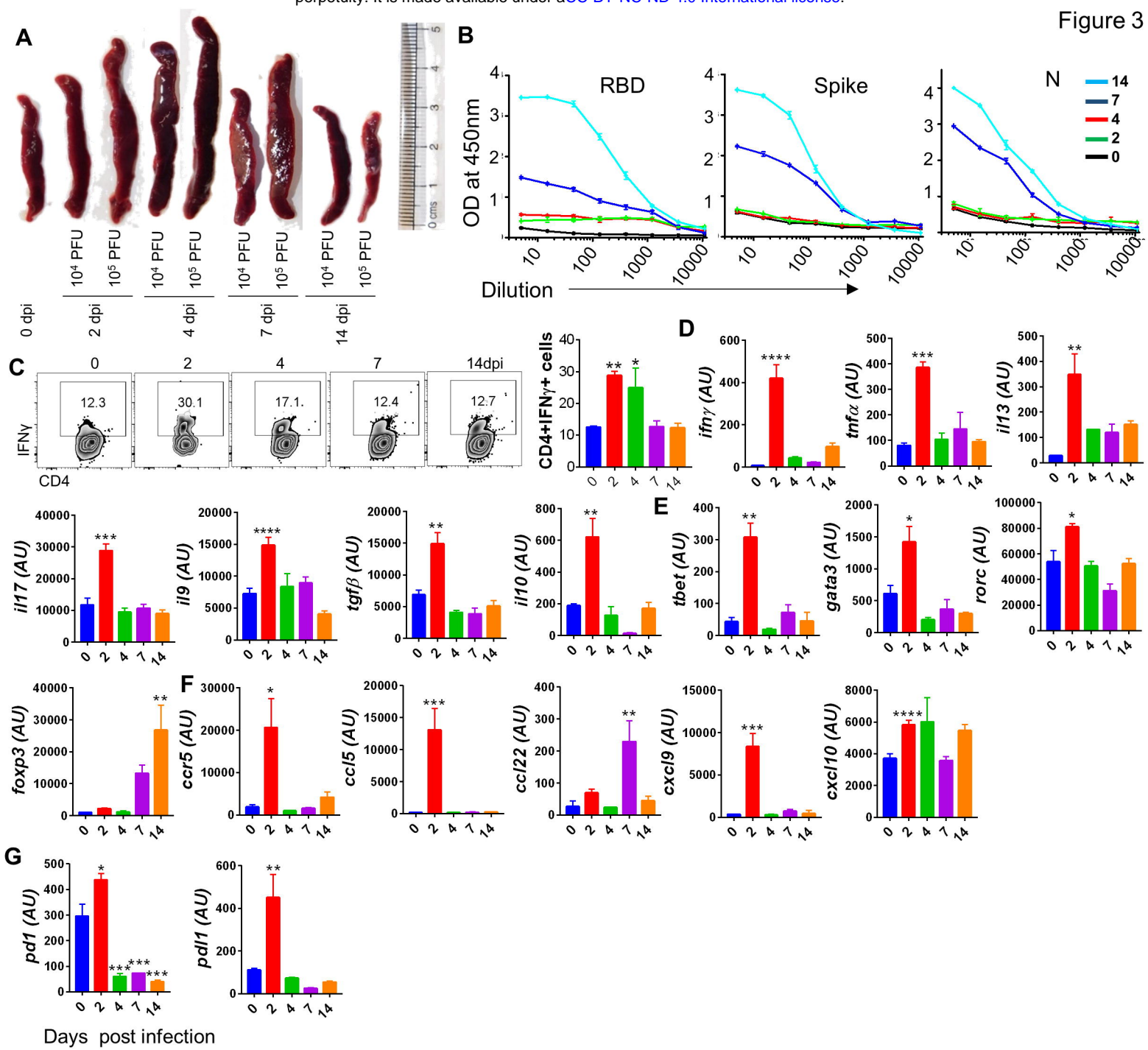
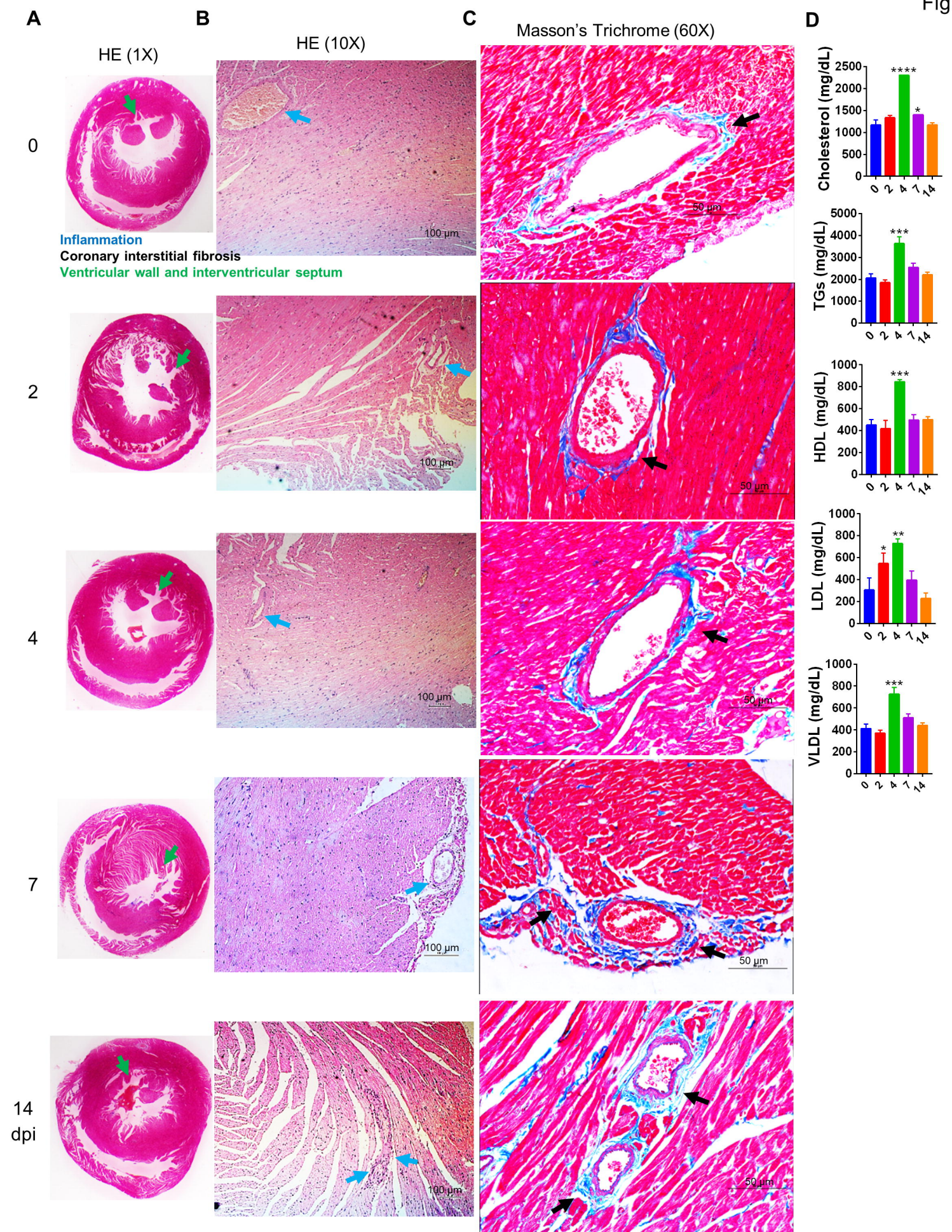


Figure 3





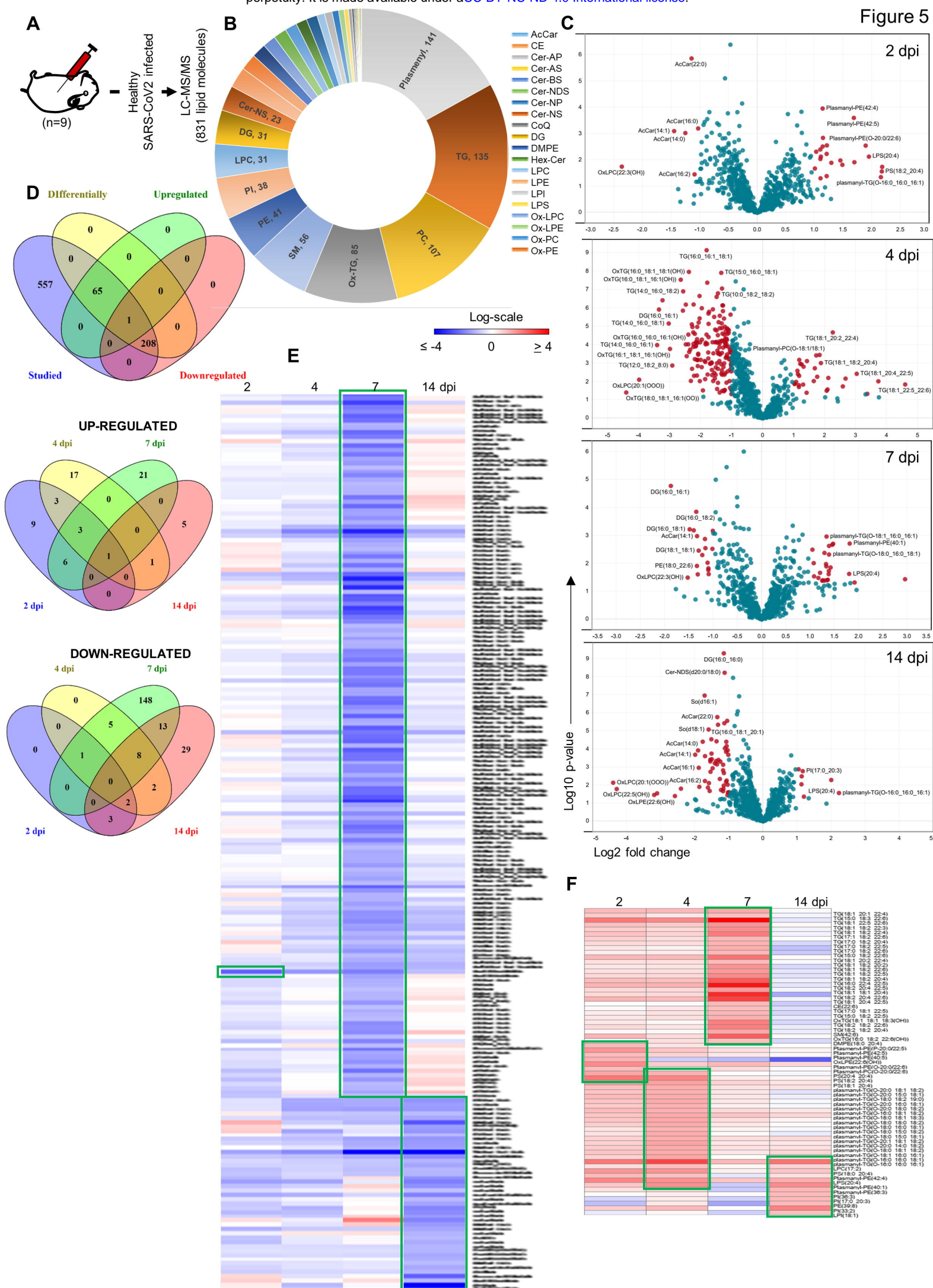


Figure 6

